

High pressure metal–silicate partitioning of Ni, Co, V, Cr, Si, and O

Rebecca A. Fischer^{a,*}, Yoichi Nakajima^{b,1}, Andrew J. Campbell^a, Daniel J. Frost^b,
Dennis Harries^c, Falko Langenhorst^c, Nobuyoshi Miyajima^b, Kilian Pollok^c,
David C. Rubie^b

^a Department of the Geophysical Sciences, University of Chicago, 5734 S Ellis Ave, Chicago, IL 60637, USA

^b Bayerisches Geoinstitut, Universität Bayreuth, D-95440 Bayreuth, Germany

^c Institut für Geowissenschaften, Friedrich-Schiller-Universität Jena, Carl-Zeiss-Promenade 10, 07745 Jena, Germany

Received 30 October 2014; accepted in revised form 19 June 2015; available online 26 June 2015

Abstract

The distributions of major and minor elements in Earth's core and mantle were primarily established by high pressure, high temperature metal–silicate partitioning during core segregation. The partitioning behaviors of moderately siderophile elements can be used to constrain the pressure–temperature conditions of core formation and the core's composition. We performed experiments to study the partitioning of Ni, Co, V, Cr, Si, and O between silicate melt and Fe-rich metallic melt in a multianvil press and diamond anvil cell, up to 100 GPa and 5700 K. Combining our new results with data from 18 previous studies, we parameterized the effects of pressure, temperature, and metallic melt composition on partitioning. Ni and Co partitioning are insensitive to composition. At low pressures, these elements become less siderophile with increasing temperature, with this trend reversing above ~45 GPa. V and Cr partitioning are much more sensitive to metallic melt composition and less sensitive to pressure. Partitioning of Si and O are insensitive to pressure, but with strong and moderate temperature dependences, respectively. Our new parameterizations of Ni and Co partitioning suggest that the Earth's distributions of these elements can be matched by single-stage core–mantle equilibration at 54 ± 5 GPa and 3300–3400 K. These conditions would result in 8.5 ± 1.4 wt% Si and 1.6 ± 0.3 wt% O in the core, compatible with the core's measured density. However, this single-stage model matches the Earth's V and Cr distributions less well. We also incorporated our parameterizations into models of multi-stage core formation over evolving pressure–temperature–oxygen fugacity conditions, reproducing the Earth's Ni and Co distributions while simultaneously producing a core whose light element composition is consistent with its density.

© 2015 The Authors. Published by Elsevier Ltd. This is an open access article under the CC BY-NC-ND license (<http://creativecommons.org/licenses/by-nc-nd/4.0/>).

1. INTRODUCTION

The present-day compositions of the Earth's core and mantle were primarily established by chemical reactions

between metal and silicate at depth during the segregation of the core (e.g., Ringwood, 1959; Li and Agee, 1996). The partitioning behaviors of most elements change at high pressures and temperatures (P and T), and knowledge of how partitioning varies with P , T , and oxygen fugacity (fO_2) is required for understanding the observed mantle composition for a chondritic bulk Earth (e.g., Li and Agee, 1996, 2001; Ohtani et al., 1997; Righter et al., 1997; Geßmann and Rubie, 1998; McDonough, 2003). Energetic impacts during the Earth's accretion caused

* Corresponding author.

E-mail address: rfischer@uchicago.edu (R.A. Fischer).

¹ Present address: Material Dynamics Laboratory, RIKEN SPring-8 Center, 1-1-1 Kouto, Sayo-cho, Sayo-gun, Hyogo, 679-5148 Japan.

large-scale melting, generating a partial or global magma ocean. Liquid metal from the impacting bodies reacted with this molten silicate as it sank through the magma ocean (Rubie et al., 2003). Many aspects of this process remain unconstrained, including the conditions of core formation and chemistry at extreme pressures and temperatures. In this study, we focus on determining the partitioning of six elements to lower mantle pressures.

Studying metal–silicate reactions can improve our understanding of the conditions of core formation. Assuming a chondritic bulk Earth, the measured mantle composition allows calculation of the core composition, and thus the effective metal–silicate partition coefficients of the bulk Earth (McDonough, 2003). These partition coefficients do not match the experimental values for most elements at 1 bar, but begin to match at high pressures and temperatures (e.g., Righter, 2003). The unique combination of pressure, temperature, and oxygen fugacity conditions that reproduce the observed partition coefficients of all elements simultaneously are those of the Earth's core formation. In addition, making some assumptions about the way that pressure, temperature, and oxygen fugacity evolved during core formation allows one to calculate the evolution of partition coefficients as the planet grows (Wade and Wood, 2005; Wood et al., 2009; Ricolleau et al., 2011; Rubie et al., 2011, 2015a; Wade et al., 2012). For example, the Earth's core is known to contain several percent of some element(s) lighter than iron, based on its seismologically inferred density (Birch, 1952). Approximately 7–10 wt% oxygen (Jeanloz and Ahrens, 1980; Fischer et al., 2011) or 8–13 wt% silicon (Lin et al., 2003; Sata et al., 2010; Mao et al., 2012; Fischer et al., 2014; Zhang et al., 2014; Tateno et al., 2015) in an iron–nickel alloy could match the outer core's density and sound velocity (though some studies disagree on this number; cf., Morard et al., 2013), but the partitioning behaviors of these elements that could account for their presence in the core need to be better understood to help discriminate between these endmember cases.

Metal–silicate reactions between liquid metal and liquid silicates at high P – T have been the subject of a large number of previous studies (e.g., Ito et al., 1995; Thibault and Walter, 1995; Hillgren et al., 1996; Li and Agee, 1996, 2001; Jana and Walker, 1997; Ohtani et al., 1997; Righter et al., 1997, 2010, 2011; Geßmann and Rubie, 1998; Bouhifd and Jephcoat, 2003, 2011; Chabot and Agee, 2003; Chabot et al., 2005; Wade and Wood, 2005; Corgne et al., 2008; Kegler et al., 2008; Cottrell et al., 2009; Mann et al., 2009; Wood et al., 2009; Ricolleau et al., 2011; Siebert et al., 2011, 2012, 2013; Wade et al., 2012; Bouhifd et al., 2013; Tsuno et al., 2013). These studies have produced a wide range of estimates of the effective pressure and temperature of core formation (see Rubie et al. (2015b) for a recent review). Most of these studies used a piston–cylinder apparatus or multianvil press, which has a pressure limit of ~ 25 GPa. However, several recent studies have suggested that core formation took place at higher effective pressures, closer to ~ 40 – 50 GPa (e.g., Wade and Wood, 2005; Kegler et al., 2008; Mann et al., 2009; Righter et al., 2011; Siebert et al., 2012). Models of

multi-stage core formation reach pressures significantly in excess of this; for example, in the modeling described in Section 4.3.2, as well as in the modeling of Rubie et al. (2015a), the final stages of core formation occur at ~ 90 GPa. Therefore it is critical to understand metal–silicate partitioning at these extreme conditions.

Only three datasets have been published on liquid metal–liquid silicate partitioning in a diamond anvil cell (Bouhifd and Jephcoat, 2003, 2011; Siebert et al., 2012, 2013), at pressures exceeding 25 GPa. These studies produced, for example, a combined total of 12 data points on Ni partitioning and 10 for Co at $P > 25$ GPa, compared to hundreds at lower pressures. (Other studies (e.g., Takafuji et al., 2005; Asahara et al., 2007; Ozawa et al., 2008, 2009) focused on solubilities of elements in liquid metal in contact with solid silicates or oxides, which are less directly relevant to core formation.) Ni and Co partitioning data at the pressures and temperatures of Earth's core formation allow for distinguishing among the range of effective core formation pressures predicted from extrapolations of multianvil press data (Bouhifd and Jephcoat, 2003, 2011). The observed partitioning behaviors of some elements at these conditions differ from simple extrapolations of their low pressure behaviors. For example, V and Cr are observed to become much more siderophile at higher P – T conditions, possibly due to interactions with oxygen in the metal (Siebert et al., 2013). The low pressure partitioning behaviors of Si and O seem to suggest mutual incompatibility in metal due to the reducing conditions necessary to put Si in the metal (e.g., Malavergne et al., 2004), but higher P – T data reveal that Si and O also both become more siderophile at these conditions (Bouhifd and Jephcoat, 2011; Siebert et al., 2012; Tsuno et al., 2013).

In this study, we performed five liquid metal–liquid silicate partitioning experiments in a diamond anvil cell at 31–100 GPa and up to 5700 K to better constrain the partitioning of Ni, Co, V, Cr, Si, and O at these extreme conditions. We also present a set of similar experiments run in a multianvil press at 15–25 GPa and 2720–2950 K. These elements were selected for the following reasons: (1) the partitioning of Ni and Co are commonly used to assess core formation conditions, and they are the best-studied elements at lower pressures (e.g., Li and Agee, 1996; Kegler et al., 2008); (2) ambiguity surrounds the partitioning of V and Cr at high pressures, due in particular to a possible change in their partitioning behaviors at ~ 30 GPa (Siebert et al., 2013), and in addition these elements are useful indicators of oxygen fugacity; and (3) Si and O are important because they are likely light elements in the Earth's core (e.g., Poirier, 1994; Allègre et al., 1995; McDonough, 2003).

2. METHODS

2.1. Diamond anvil cell experiments

Five experiments were performed in a laser-heated diamond anvil cell at the University of Chicago. The metallic starting materials were iron-rich alloys synthesized in a piston–cylinder apparatus, containing small amounts of

nickel, cobalt, and vanadium, with or without silicon (metallic starting compositions are listed in [Table A.1](#)). The silicate was either San Carlos olivine or ringwoodite synthesized from a natural olivine, both approximately $(\text{Mg}_{0.9}\text{Fe}_{0.1})_2\text{SiO}_4$. The pressure, temperature, and oxygen fugacity of each diamond cell experiment is listed in [Table 1](#), with starting materials listed in [Table A.2](#). Oxygen fugacity in log units relative to the iron–wüstite (IW) buffer is defined as:

$$\Delta IW = 2 \log_{10} \left(\frac{a_{\text{FeO}}^{\text{sil}}}{a_{\text{FeO}}^{\text{met}}} \right) \quad (1)$$

where $a_{\text{FeO}}^{\text{sil}}$ is the activity of FeO in the silicate melt and $a_{\text{Fe}}^{\text{met}}$ is the activity of Fe in the metal, approximated here as their mole fractions. Incorporating activities for Fe and FeO that differ from unity based on a thermodynamic model (Frost et al., 2010) results in a calculated oxygen fugacity that is higher by ~ 0.4 log units, in agreement with previous studies (Bouhifd and Jephcoat, 2011; Siebert et al., 2012). Two experiments were run at almost identical conditions, with the only difference being the silicon content of the metal. Pressures were determined by ruby fluorescence measurements at room temperature (Mao et al., 1978) before and after each experiment, with additional thermal pressure (15–20% of the pre-heating pressure) estimated based on two additional experiments with the same geometry run with in situ synchrotron X-ray diffraction. Uncertainties in pressure were determined based on uncertainties in the ruby measurement and the thermal pressure correction.

Samples were loaded in rhenium gaskets preindented to ~ 28 GPa, or in stainless steel gaskets preindented to ~ 18 GPa. The metallic starting material was loaded as a thin foil, between flakes of silicate powder, with a few ruby grains added as pressure markers. The sample assembly was oven dried at $\sim 90^\circ\text{C}$ after loading but before closing the cell to remove any moisture. Samples were compressed to a target pressure, then laser-heated from both sides with a 1064 nm Yb-doped fiber laser, which created laser-heated spots $\sim 30\text{ }\mu\text{m}$ in diameter. Heating lasted ~ 10 min, with the temperature gradually increased throughout and the laser intensity on each side adjusted to minimize axial temperature gradients. The sample was quenched after holding it at the target temperature for at least ~ 15 s.

In addition to live time spectroradiometric temperature measurements, two-dimensional temperature maps of the laser-heated spot were measured using a four-color temperature mapping system (Campbell, 2008; Fischer and Campbell, 2010). In this method, images of the laser-heated spot are captured at four wavelengths and spatially correlated. At each pixel, a four-color fit to the Planck radiation function is performed using the greybody approximation. An example of one of our temperature maps is shown in Fig. 1. Mapping the temperature gradients allows for better understanding of the chemistry and morphology of our recovered samples. Quoted temperatures are the average of the temperatures in the hottest region of the temperature map within the diameter of the melt, measured on both sides of the sample. Uncertainties in temperature include the standard deviations of these values and an analytical uncertainty.

Table 1
Pressures, temperatures, oxygen fugacities, and partition and exchange coefficients for our diamond anvil cell (DAC) experiments and multianvil press (MAP) experiments. Oxygen fugacity is calculated assuming ideality.

| Apparatus | | | | | | | | | |
|---|---|---|---|---|---|---|---|---|---|
| DAC | DAC | DAC | DAC | DAC | DAC | DAC | DAC | DAC | DAC |
| 31 ± 5 | 39 ± 5 | 56 ± 6 | 57 ± 6 | 100 ± 8 | 250 ± 1.0 | 250 ± 1.0 | 250 ± 1.0 | 250 ± 1.0 | 250 ± 1.0 |
| 4560 ± 140 | 4440 ± 160 | 4360 ± 140 | 4440 ± 160 | 5700 ± 500 | 2740 ± 100 | 2740 ± 100 | 2740 ± 100 | 2740 ± 100 | 2740 ± 100 |
| -12.0 | -12.0 | -1.1 | -0.9 | -1.1 | -2.2 | -2.4 | -2.4 | -2.4 | -2.4 |
| O ₂ (ΔW) | O ₂ (ΔW) | O ₂ (ΔW) | O ₂ (ΔW) | O ₂ (ΔW) | O ₂ (ΔW) | O ₂ (ΔW) | O ₂ (ΔW) | O ₂ (ΔW) | O ₂ (ΔW) |
| 12 ± 4 | 13 ± 2 | 7 ± 3 | 5.1 ± 0.6 | 4.9 ± 0.6 | 150 ± 30 | 190 ± 80 | 140 ± 90 | 180 ± 80 | 140 ± 90 |
| graphite/Al ₂ O ₃ | graphite/Al ₂ O ₃ | graphite/Al ₂ O ₃ | graphite/Al ₂ O ₃ | graphite/Al ₂ O ₃ | 100 ± 30 | 120 ± 80 | 90 ± 30 | 120 ± 80 | 90 ± 30 |
| 0.43 ± 0.15 | 0.43 ± 0.15 | 0.5 ± 0.3 | 0.5 ± 0.3 | 0.86 ± 0.11 | 0.216 ± 0.015 | 0.30 ± 0.03 | 0.30 ± 0.03 | 0.42 ± 0.11 | 0.21 ± 0.05 |
| graphite/Al ₂ O ₃ | graphite/Al ₂ O ₃ | graphite/Al ₂ O ₃ | graphite/Al ₂ O ₃ | graphite/Al ₂ O ₃ | graphite/Al ₂ O ₃ | graphite/Al ₂ O ₃ | graphite/Al ₂ O ₃ | graphite/Al ₂ O ₃ | graphite/Al ₂ O ₃ |
| 1.7 ± 0.8 | 1.7 ± 0.8 | 2 ± 3 | 1.7 ± 0.8 | 0.352 ± 0.012 | 0.08 ± 0.03 | 0.101 ± 0.009 | 0.14 ± 0.03 | 0.06 ± 0.03 | 0.08 ± 0.03 |
| graphite/Al ₂ O ₃ | graphite/Al ₂ O ₃ | graphite/Al ₂ O ₃ | graphite/Al ₂ O ₃ | graphite/Al ₂ O ₃ | graphite/Al ₂ O ₃ | graphite/Al ₂ O ₃ | graphite/Al ₂ O ₃ | graphite/Al ₂ O ₃ | graphite/Al ₂ O ₃ |
| 0.129 ± 0.017 | 0.129 ± 0.017 | 0.098 ± 0.008 | 0.098 ± 0.008 | 0.352 ± 0.012 | 0.08 ± 0.03 | 0.101 ± 0.009 | 0.14 ± 0.03 | 0.06 ± 0.03 | 0.08 ± 0.03 |
| graphite/Al ₂ O ₃ | graphite/Al ₂ O ₃ | graphite/Al ₂ O ₃ | graphite/Al ₂ O ₃ | graphite/Al ₂ O ₃ | graphite/Al ₂ O ₃ | graphite/Al ₂ O ₃ | graphite/Al ₂ O ₃ | graphite/Al ₂ O ₃ | graphite/Al ₂ O ₃ |
| 3.08 ± 0.12 | 3.08 ± 0.12 | 3.6 ± 0.3 | 3.6 ± 0.3 | 3.6 ± 0.3 | 13 ± 2 | 23 ± 3 | 16.4 ± 1.0 | 24 ± 2 | 14 ± 4 |
| graphite/Al ₂ O ₃ | graphite/Al ₂ O ₃ | graphite/Al ₂ O ₃ | graphite/Al ₂ O ₃ | graphite/Al ₂ O ₃ | graphite/Al ₂ O ₃ | graphite/Al ₂ O ₃ | graphite/Al ₂ O ₃ | graphite/Al ₂ O ₃ | graphite/Al ₂ O ₃ |
| 0.60 ± 0.15 | 0.60 ± 0.15 | 0.53 ± 0.10 | 0.53 ± 0.10 | 0.53 ± 0.10 | 1.07 ± 0.12 | 0.92 ± 0.18 | 0.92 ± 0.18 | 1.07 ± 0.14 | 0.92 ± 0.18 |
| graphite/Al ₂ O ₃ | graphite/Al ₂ O ₃ | graphite/Al ₂ O ₃ | graphite/Al ₂ O ₃ | graphite/Al ₂ O ₃ | graphite/Al ₂ O ₃ | graphite/Al ₂ O ₃ | graphite/Al ₂ O ₃ | graphite/Al ₂ O ₃ | graphite/Al ₂ O ₃ |
| 0.31 ± 0.09 | 0.31 ± 0.09 | 0.41 ± 0.18 | 0.41 ± 0.18 | 0.41 ± 0.18 | 0.88 ± 0.16 | 0.7 ± 0.3 | 0.7 ± 0.4 | 0.83 ± 0.19 | 0.7 ± 0.3 |
| graphite/Al ₂ O ₃ | graphite/Al ₂ O ₃ | graphite/Al ₂ O ₃ | graphite/Al ₂ O ₃ | graphite/Al ₂ O ₃ | graphite/Al ₂ O ₃ | graphite/Al ₂ O ₃ | graphite/Al ₂ O ₃ | graphite/Al ₂ O ₃ | graphite/Al ₂ O ₃ |
| -1.10 ± 0.15 | -1.10 ± 0.15 | -0.89 ± 0.07 | -0.89 ± 0.07 | -0.89 ± 0.07 | -2.33 ± 0.11 | -2.35 ± 0.05 | -2.35 ± 0.05 | -2.40 ± 0.19 | -2.35 ± 0.05 |
| graphite/Al ₂ O ₃ | graphite/Al ₂ O ₃ | graphite/Al ₂ O ₃ | graphite/Al ₂ O ₃ | graphite/Al ₂ O ₃ | graphite/Al ₂ O ₃ | graphite/Al ₂ O ₃ | graphite/Al ₂ O ₃ | graphite/Al ₂ O ₃ | graphite/Al ₂ O ₃ |
| -0.2 ± 0.6 | -0.2 ± 0.6 | -0.2 ± 0.6 | -0.2 ± 0.6 | -0.2 ± 0.6 | -3.3 ± 0.2 | -3.42 ± 0.10 | -3.42 ± 0.10 | -3.5 ± 0.15 | -3.42 ± 0.10 |
| graphite/Al ₂ O ₃ | graphite/Al ₂ O ₃ | graphite/Al ₂ O ₃ | graphite/Al ₂ O ₃ | graphite/Al ₂ O ₃ | graphite/Al ₂ O ₃ | graphite/Al ₂ O ₃ | graphite/Al ₂ O ₃ | graphite/Al ₂ O ₃ | graphite/Al ₂ O ₃ |
| -1.87 ± 0.07 | -1.87 ± 0.07 | -2.37 ± 0.13 | -2.37 ± 0.13 | -2.37 ± 0.13 | -0.4 ± 0.3 | -0.4 ± 0.3 | -0.4 ± 0.3 | -0.4 ± 0.3 | -0.4 ± 0.3 |
| graphite/Al ₂ O ₃ | graphite/Al ₂ O ₃ | graphite/Al ₂ O ₃ | graphite/Al ₂ O ₃ | graphite/Al ₂ O ₃ | graphite/Al ₂ O ₃ | graphite/Al ₂ O ₃ | graphite/Al ₂ O ₃ | graphite/Al ₂ O ₃ | graphite/Al ₂ O ₃ |
| -0.19 ± 0.05 | -0.19 ± 0.05 | 0.00 ± 0.07 | 0.00 ± 0.07 | 0.00 ± 0.07 | -0.4 ± 0.3 | -0.5 ± 0.2 | -0.5 ± 0.2 | -0.5 ± 0.2 | -0.5 ± 0.2 |
| graphite/Al ₂ O ₃ | graphite/Al ₂ O ₃ | graphite/Al ₂ O ₃ | graphite/Al ₂ O ₃ | graphite/Al ₂ O ₃ | graphite/Al ₂ O ₃ | graphite/Al ₂ O ₃ | graphite/Al ₂ O ₃ | graphite/Al ₂ O ₃ | graphite/Al ₂ O ₃ |
| -0.05 ± 0.04 | -0.05 ± 0.04 | -0.21 ± 0.13 | -0.21 ± 0.13 | -0.21 ± 0.13 | -0.4 ± 0.3 | -0.5 ± 0.2 | -0.5 ± 0.2 | -0.5 ± 0.2 | -0.5 ± 0.2 |
| graphite/Al ₂ O ₃ | graphite/Al ₂ O ₃ | graphite/Al ₂ O ₃ | graphite/Al ₂ O ₃ | graphite/Al ₂ O ₃ | graphite/Al ₂ O ₃ | graphite/Al ₂ O ₃ | graphite/Al ₂ O ₃ | graphite/Al ₂ O ₃ | graphite/Al ₂ O ₃ |
| -0.39 ± 0.08 | -0.39 ± 0.08 | -0.36 ± 0.08 | -0.36 ± 0.08 | -0.36 ± 0.08 | -3.5 ± 0.15 | -3.54 ± 0.10 | -3.54 ± 0.10 | -3.6 ± 0.18 | -3.54 ± 0.10 |
| graphite/Al ₂ O ₃ | graphite/Al ₂ O ₃ | graphite/Al ₂ O ₃ | graphite/Al ₂ O ₃ | graphite/Al ₂ O ₃ | graphite/Al ₂ O ₃ | graphite/Al ₂ O ₃ | graphite/Al ₂ O ₃ | graphite/Al ₂ O ₃ | graphite/Al ₂ O ₃ |
| -0.95 ± 0.09 | -0.95 ± 0.09 | -1.11 ± 0.04 | -1.11 ± 0.04 | -1.11 ± 0.04 | -2.49 ± 0.06 | -2.49 ± 0.06 | -2.49 ± 0.06 | -2.49 ± 0.06 | -2.49 ± 0.06 |
| graphite/Al ₂ O ₃ | graphite/Al ₂ O ₃ | graphite/Al ₂ O ₃ | graphite/Al ₂ O ₃ | graphite/Al ₂ O ₃ | graphite/Al ₂ O ₃ | graphite/Al ₂ O ₃ | graphite/Al ₂ O ₃ | graphite/Al ₂ O ₃ | graphite/Al ₂ O ₃ |
| -1.08 ± 0.15 | -1.08 ± 0.15 | -1.11 ± 0.04 | -1.11 ± 0.04 | -1.11 ± 0.04 | -2.49 ± 0.06 | -2.49 ± 0.06 | -2.49 ± 0.06 | -2.49 ± 0.06 | -2.49 ± 0.06 |
| graphite/Al ₂ O ₃ | graphite/Al ₂ O ₃ | graphite/Al ₂ O ₃ | graphite/Al ₂ O ₃ | graphite/Al ₂ O ₃ | graphite/Al ₂ O ₃ | graphite/Al ₂ O ₃ | graphite/Al ₂ O ₃ | graphite/Al ₂ O ₃ | graphite/Al ₂ O ₃ |
| -2.13 ± 0.12 | -2.13 ± 0.12 | -2.46 ± 0.10 | -2.46 ± 0.10 | -2.46 ± 0.10 | -2.49 ± 0.06 | -2.49 ± 0.06 | -2.49 ± 0.06 | -2.49 ± 0.06 | -2.49 ± 0.06 |
| graphite/Al ₂ O ₃ | graphite/Al ₂ O ₃ | graphite/Al ₂ O ₃ | graphite/Al ₂ O ₃ | graphite/Al ₂ O ₃ | graphite/Al ₂ O ₃ | graphite/Al ₂ O ₃ | graphite/Al ₂ O ₃ | graphite/Al ₂ O ₃ | graphite/Al ₂ O ₃ |
| -0.78 ± 0.13 | -0.78 ± 0.13 | -0.86 ± 0.08 | -0.86 ± 0.08 | -0.86 ± 0.08 | 0.65 ± 0.19 | 0.65 ± 0.19 | 0.65 ± 0.19 | 0.65 ± 0.19 | 0.65 ± 0.19 |
| graphite/Al ₂ O ₃ | graphite/Al ₂ O ₃ | graphite/Al ₂ O ₃ | graphite/Al ₂ O ₃ | graphite/Al ₂ O ₃ | graphite/Al ₂ O ₃ | graphite/Al ₂ O ₃ | graphite/Al ₂ O ₃ | graphite/Al ₂ O ₃ | graphite/Al ₂ O ₃ |
| 0.83 ± 0.13 | 0.83 ± 0.13 | 0.70 ± 0.13 | 0.70 ± 0.13 | 0.70 ± 0.13 | 0.88 ± 0.09 | 0.88 ± 0.09 | 0.88 ± 0.09 | 0.88 ± 0.09 | 0.88 ± 0.09 |
| graphite/Al ₂ O ₃ | graphite/Al ₂ O ₃ | graphite/Al ₂ O ₃ | graphite/Al ₂ O ₃ | graphite/Al ₂ O ₃ | graphite/Al ₂ O ₃ | graphite/Al ₂ O ₃ | graphite/Al ₂ O ₃ | graphite/Al ₂ O ₃ | graphite/Al ₂ O ₃ |
| 0.75 ± 0.18 | 0.75 ± 0.18 | 0.75 ± 0.18 | 0.75 ± 0.18 | 0.75 ± 0.18 | 0.83 ± 0.14 | 0.83 ± 0.14 | 0.83 ± 0.14 | 0.83 ± 0.14 | 0.83 ± 0.14 |
| graphite/Al ₂ O ₃ | graphite/Al ₂ O ₃ | graphite/Al ₂ O ₃ | graphite/Al ₂ O ₃ | graphite/Al ₂ O ₃ | graphite/Al ₂ O ₃ | graphite/Al ₂ O ₃ | graphite/Al ₂ O ₃ | graphite/Al ₂ O ₃ | graphite/Al ₂ O ₃ |
| 0.86 ± 0.10 | 0.86 ± 0.10 | 0.86 ± 0.10 | 0.86 ± 0.10 | 0.86 ± 0.10 | 0.86 ± 0.16 | 0.86 ± 0.16 | 0.86 ± 0.16 | 0.86 ± 0.16 | 0.86 ± 0.16 |
| graphite/Al ₂ O ₃ | graphite/Al ₂ O ₃ | graphite/Al ₂ O ₃ | graphite/Al ₂ O ₃ | graphite/Al ₂ O ₃ | graphite/Al ₂ O ₃ | graphite/Al ₂ O ₃ | graphite/Al ₂ O ₃ | graphite/Al ₂ O ₃ | graphite/Al ₂ O ₃ |
| 0.75 ± 0.18 | 0.75 ± 0.18 | 0.75 ± 0.18 | 0.75 ± 0.18 | 0.75 ± 0.18 | 0.86 ± 0.16 | 0.86 ± 0.16 | 0.86 ± 0.16 | 0.86 ± 0.16 | 0.86 ± 0.16 |
| graphite/Al ₂ O ₃ | graphite/Al ₂ O ₃ | graphite/Al ₂ O ₃ | graphite/Al ₂ O ₃ | graphite/Al ₂ O ₃ | graphite/Al ₂ O ₃ | graphite/Al ₂ O ₃ | graphite/Al ₂ O ₃ | graphite/Al ₂ O ₃ | graphite/Al ₂ O ₃ |
| 0.86 ± 0.10 | 0.86 ± 0.10 | 0.86 ± 0.10 | 0.86 ± 0.10 | 0.86 ± 0.10 | 0.86 ± 0.16 | 0.86 ± 0.16 | 0.86 ± 0.16 | 0.86 ± 0.16 | 0.86 ± 0.16 |
| graphite/Al ₂ O ₃ | graphite/Al ₂ O ₃ | graphite/Al ₂ O ₃ | graphite/Al ₂ O ₃ | graphite/Al ₂ O ₃ | graphite/Al ₂ O ₃ | graphite/Al ₂ O ₃ | graphite/Al ₂ O ₃ | graphite/Al ₂ O ₃ | graphite/Al ₂ O ₃ |
| 0.86 ± 0.10 | 0.86 ± 0.10 | 0.86 ± 0.10 | 0.86 ± 0.10 | 0.86 ± 0.10 | 0.86 ± 0.16 | 0.86 ± 0.16 | 0.86 ± 0.16 | 0.86 ± 0.16 | 0.86 ± 0.16 |
| graphite/Al ₂ O ₃ | graphite/Al ₂ O ₃ | graphite/Al ₂ O ₃ | graphite/Al ₂ O ₃ | graphite/Al ₂ O ₃ | graphite/Al ₂ O ₃ | graphite/Al ₂ O ₃ | graphite/Al ₂ O ₃ | graphite/Al ₂ O ₃ | graphite/Al ₂ O ₃ |
| 0.86 ± 0.10 | 0.86 ± 0.10 | 0.86 ± 0.10 | 0.86 ± 0.10 | 0.86 ± 0.10 | 0.86 ± 0.16 | 0.86 ± 0.16 | 0.86 ± 0.16 | 0.86 ± 0.16 | 0.86 ± 0.16 |
| graphite/Al ₂ O ₃ | graphite/Al ₂ O ₃ | graphite/Al ₂ O ₃ | graphite/Al ₂ O ₃ | graphite/Al ₂ O ₃ | graphite/Al ₂ O ₃ | graphite/Al ₂ O ₃ | graphite/Al ₂ O ₃ | graphite/Al ₂ O ₃ | graphite/Al ₂ O ₃ |
| 0.86 ± 0.10 | 0.86 ± 0.10 | 0.86 ± 0.10 | 0.86 ± 0.10 | 0.86 ± 0.10 | 0.86 ± 0.16 | 0.86 ± 0.16 | 0.86 ± 0.16 | 0.86 ± 0.16 | 0.86 ± 0.16 |
| graphite/Al ₂ O ₃ | graphite/Al ₂ O ₃ | graphite/Al ₂ O ₃ | graphite/Al ₂ O ₃ | graphite/Al ₂ O ₃ | graphite/Al ₂ O ₃ | graphite/Al ₂ O ₃ | graphite/Al ₂ O ₃ | graphite/Al ₂ O ₃ | graphite/Al ₂ O ₃ |
| 0.86 ± 0.10 | 0.86 ± 0.10 | 0.86 ± 0.10 | 0.86 ± 0.10 | 0.86 ± 0.10 | 0.86 ± 0.16 | 0.86 ± 0.16 | 0.86 ± 0.16 | 0.86 ± 0.16 | 0.86 ± 0.16 |
| graphite/Al ₂ O ₃ | graphite/Al ₂ O ₃ | graphite/Al ₂ O ₃ | graphite/Al ₂ O ₃ | graphite/Al ₂ O ₃ | graphite/Al ₂ O ₃ | graphite/Al ₂ O ₃ | graphite/Al ₂ O ₃ | graphite/Al ₂ O ₃ | graphite/Al ₂ O ₃ |
| 0.86 ± 0.10 | 0.86 ± 0.10 | 0.86 ± 0.10 | 0.86 ± 0.10 | 0.86 ± 0.10 | 0.86 ± 0.16 | 0.86 ± 0.16 | 0.86 ± 0.16 | 0.86 ± 0.16 | 0.86 ± 0.16 |
| graphite/Al ₂ O ₃ | graphite/Al ₂ O ₃ | graphite/Al ₂ O ₃ | graphite/Al ₂ O ₃ | graphite/Al ₂ O ₃ | graphite/Al ₂ O ₃ | graphite/Al ₂ O ₃ | graphite/Al ₂ O ₃ | graphite/Al ₂ O ₃ | graphite/Al ₂ O ₃ |
| 0.86 ± 0.10 | 0.86 ± 0.10 | 0.86 ± 0.10 | 0.86 ± 0.10 | 0.86 ± 0.10 | 0.86 ± 0.16 | 0.86 ± 0.16 | 0.86 ± 0.16 | 0.86 ± 0.16 | 0.86 ± 0.16 |
| graphite/Al ₂ O ₃ | graphite/Al ₂ O ₃ | graphite/Al ₂ O ₃ | graphite/Al ₂ O ₃ | graphite/Al ₂ O ₃ | graphite/Al ₂ O ₃ | graphite/Al ₂ O ₃ | graphite/Al ₂ O ₃ | graphite/Al ₂ O ₃ | graphite/Al ₂ O ₃ |
| 0.86 ± 0.10 | 0.86 ± 0.10 | 0.86 ± 0.10 | 0.86 ± 0.10 | 0.86 ± 0.10 | 0.86 ± 0.16 | 0.86 ± 0.16 | 0.86 ± 0.16 | 0.86 ± 0.16 | 0.86 ± 0.16 |
| graphite/Al ₂ O ₃ | graphite/Al ₂ O ₃ | graphite/Al ₂ O ₃ | graphite/Al ₂ O ₃ | graphite/Al ₂ O ₃ | graphite/Al ₂ O ₃ | graphite/Al ₂ O ₃ | graphite/Al ₂ O ₃ | graphite/Al ₂ O ₃ | graphite/Al ₂ O ₃ |
| 0.86 ± 0.10 | 0.86 ± 0.10 | 0.86 ± 0.10 | 0.86 ± 0.10 | 0.86 ± 0.10 | 0.86 ± 0.16 | 0.86 ± 0.16 | 0.86 ± 0.16 | 0.86 ± 0.16 | 0.86 ± 0.16 |
| graphite/Al ₂ O ₃ | graphite/Al ₂ O ₃ | graphite/Al ₂ O ₃ | graphite/Al ₂ O ₃ | graphite/Al ₂ O ₃ | graphite/Al ₂ O ₃ | graphite/Al ₂ O ₃ | graphite/Al ₂ O ₃ | graphite/Al ₂ O ₃ | graphite/Al ₂ O ₃ |
| 0.86 ± 0.10 | 0.86 ± 0.10 | 0.86 ± 0.10 | 0.86 ± 0.10 | 0.86 ± 0.10 | 0.86 ± 0.16 | 0.86 ± 0.16 | 0.86 ± 0.16 | 0.86 ± 0.16 | 0.86 ± 0.16 |
| graphite/Al ₂ O ₃ | graphite/Al ₂ O ₃ | graphite/Al ₂ O ₃ | graphite/Al ₂ O ₃ | graphite/Al ₂ O ₃ | graphite/Al ₂ O ₃ | graphite/Al ₂ O ₃ | graphite/Al ₂ O ₃ | graphite/Al ₂ O ₃ | graphite/Al ₂ O ₃ |
| 0.86 ± 0.10 | 0.86 ± 0.10 | 0.86 ± 0.10 | 0.86 ± 0.10 | 0.86 ± 0.10 | 0.86 ± 0.16 | 0.86 ± 0.16 | 0.86 ± 0.16 | 0.86 ± 0.16 | 0.86 ± 0.16 |
| graphite/Al ₂ O ₃ | graphite/Al ₂ O ₃ | graphite/Al ₂ O ₃ | graphite/Al ₂ O ₃ | | | | | | |

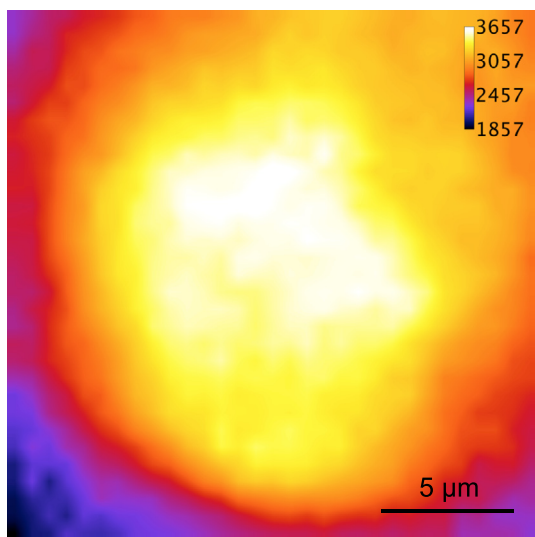


Fig. 1. Two-dimensional temperature map of the laser-heated spot in one of our diamond anvil cell experiments, performed at 39 GPa.

2.2. Analyses of diamond cell runs

Run products of our diamond anvil cell experiments were sectioned using a 30 keV Ga^+ focused ion beam (FIB) instrument at Friedrich Schiller University of Jena (FEI Quanta 3D FEG). During sectioning the samples were monitored by scanning electron microscopy using back-scattered electrons to precisely locate the centers of the laser-heated spots. Sections $\sim 2 \mu\text{m}$ thick were removed from the centers via an in situ micromanipulator, mounted on Cu grids using ion beam-induced Pt deposition, and thinned to $\sim 150 \text{ nm}$ thickness by the Ga^+ ion beam for analysis by energy dispersive X-ray microanalysis (EDX) in a transmission electron microscope (TEM). They were later thinned further to 60–80 nm thickness for electron energy loss spectroscopy (EELS). Thinning took place at decreasing ion beam currents of 300 to 50 pA and incident angles of less than $\sim 4^\circ$ relative to the foil surface. In some cases final thinning was done using 5 keV Ga^+ ions to minimize Ga implantation.

Analytical transmission electron microscopy was performed at the University of Bayreuth using a Philips CM20 field emission gun scanning TEM operating at 200 kV. A large (0.5–2.0 μm) beam was used to average over quench textures (Section 3), while a small beam was used to investigate individual mineral grains and compositional gradients. Quenched silicate and metallic melts were each analyzed in 4–8 spots by EDX. Evaluation of TEM-EDX spectra involved the use of experimentally-calibrated k-factors of oxygen, magnesium, silicon, calcium, chromium, and iron (van Cappellen, 1990), k-factors estimated from theory for vanadium, manganese, cobalt, and nickel, and an absorption correction based on approximate densities and sample thicknesses (see the supplemental text for details). To measure trace elements, we accumulated several EDX spectra from the silicate melt and the iron alloy with longer acquisition times ($\sim 600 \text{ s}$) and higher count rates, up to 5.5 kcps (dead

time up to 30% for a pure Ge solid state detector). Typical detection limits are 240 ppm for V in metal and 250 ppm for CrO in silicate, for example, so our reported peaks are statistically significant. Uncertainties were mainly calculated as standard deviations of multiple measurements, which capture the dominant sources of uncertainty. Further details about the detection limits and analytical uncertainties in our EDX measurements may be found in the supplemental text.

Following further FIB thinning, the metal was reanalyzed by EELS to determine the Fe/C and Fe/O ratios. The FIB lamellae were cleaned by a plasma cleaning system prior to TEM-EELS analyses. We calibrated ratios of partial ionization cross-sections of carbon and oxygen against iron in EELS analysis in an FEI Titan G2 80-200 S/TEM equipped with an energy filter system, Gatan GIF Quantum SE, operating at 200 kV under an oil-free vacuum system. The quantification of the EELS analyses followed the procedure described by Miyajima et al. (2009), using experimentally determined ratios of partial cross sections of C K and O K edges against the Fe L edge versus sample thickness, which were calibrated with synthetic $\text{Fe}_{0.94}\text{O}$ and Fe_3C samples. The Fe_3C standard was synthesized at 1–2 GPa and $<1100^\circ\text{C}$. The coexisting bcc-Fe metal contained $<7 \text{ at\%}$ carbon, so we can assume the carbide phase is almost stoichiometric, 23–25 at% carbon (Walker et al., 2013). Detection limits in EELS measurements depend strongly on the thickness of the sample. For samples 60–80 nm thick, detection limits are $\sim 0.8 \text{ at\%}$ for oxygen and $\sim 0.6 \text{ at\%}$ for carbon (Miyajima et al., 2009). Thickness effects were corrected using a linear relation between the partial cross-section ratio of the inelastic electron scattering and the sample thickness without corrections of multiple scatterings (Miyajima et al., 2009).

2.3. Multianvil press experiments and analyses

We also ran 15 experiments in a multianvil press at pressures of 15–25 GPa and temperatures of 2720–2950 K at the University of Bayreuth. Starting materials were powdered mixtures of metal and silicate. The metals were mixtures of Fe or Fe–9 wt% Si alloy and trace amounts of Ni, Co, V, Cr, and/or W (2–5 wt% each). In three experiments, a larger amount of Ni (20 wt%) was added. The starting silicates were either natural San Carlos olivine or synthetic olivines with varying iron contents ($(\text{Mg}_{1-x}\text{Fe}_x)_2\text{SiO}_4$ with $x = 0.05\text{--}0.3$). The samples were packed into single crystal MgO capsules. The pressure, temperature, and oxygen fugacity of each experiment are listed in Table 1, with starting materials and durations listed in Table A.2. Again, calculating oxygen fugacity using a thermodynamic model for activity coefficients (Frost et al., 2010) results in a value that is higher by $\sim 0.4 \text{ log units}$, in agreement with previous studies (e.g., Cottrell et al., 2009; Siebert et al., 2011; Bouhifd et al., 2013).

The pressure medium was a 10 mm edge length Cr_2O_3 -doped MgO octahedron, with 4 mm or 5 mm truncated edge length tungsten-carbide anvils. A cylindrical LaCrO_3 heater was used. Temperature was measured by a W–Re thermocouple type-D (except for one run), whose

junction was located at the top of the sample capsule. In one run, two capsules were loaded together but without a thermocouple, and temperature was estimated from the input power to the heater. The duration time at a target temperature was 2–10 min, then the sample was quenched by turning off the electric power to the heater. Uncertainties in pressure and temperature were approximately ± 1 GPa and ± 100 K, respectively, based on the reproducibility of phase transitions in Mg_2SiO_4 at 1873 K and on the power–temperature relationship. Note that the uncertainty in pressure is not as well defined at higher temperatures due to a lack of calibration.

Following each experiment, the sample was polished and then analyzed by an electron microprobe (JXA-8200) with wavelength dispersive X-ray spectroscopy. An accelerating voltage of 15 kV and a beam current of 20–50 nA were used for both metal and silicate phases. A defocused beam was used with a diameter of 5–30 μm for quenched metal and silicate melts. A typical counting time for each element peak was 20–30 s for major elements (Fe, Mg, Si) and 40–60 s for trace elements, including Si and O in the metal. A series of metals and oxides were used as internal standards. With the present analytical methods, the detection limits for trace elements were 50–100 ppm (except for W, whose detection limit was 100–200 ppm). To obtain bulk compositions of quenched metallic and silicate melts, multiple analyses with a defocused/raster-scanned electron beam (5–30 μm) were averaged. The size of the beam was changed, depending on the size and shape of the metal and silicate regions, in order to avoid contamination by adjacent phases.

3. RESULTS

Compositions of the quenched silicate and metallic melts from our five diamond anvil cell experiments and our 15 multianvil press experiments are reported in Table A.2. Uncertainties are reported as the standard deviations of several TEM-EDX, EELS, or microprobe measurements.

The starting metal in our experiments contained neither oxygen nor carbon (Tables A.1 and A.2). The oxygen in the quenched metallic melt originated from the silicate melt, while the carbon in diamond cell experiments likely diffused in from the diamond anvils. Carbon is present in the metallic melt but is below detection limits in the silicate melt. It is known to be strongly siderophile at pressures up to 5 GPa (Dasgupta et al., 2013; Chi et al., 2014; Li et al., 2015), so its absence in the silicate indicates that the carbon was in the system during the high P – T experiments and was not introduced as a contaminant during analyses. The light element content of the metal increases with increasing temperature and pressure, reaching 11.3 wt% O, 8.8 wt% Si, and 0.9 wt% C at 100 GPa and 5700 K (Table A.2).

Our diamond anvil cell experiments result in similar oxidation states (relative to the IW buffer) regardless of the small differences in composition of the starting material (Table A.2), and in general diamond anvil cell experiments produce higher oxidation states than multianvil press experiments (Table A.3). Siebert et al. (2012, 2013) similarly report uniform high oxidation states in their diamond cell experiments. This phenomenon can be explained by the

increased partitioning of Si into the metal relative to Fe at higher pressures and temperatures (Section 4.1.3), which increases the FeO content of the silicate and thus increases the oxidation state relative to the IW buffer.

Images of two of our recovered diamond anvil cell samples are shown in Fig. 2. Their morphology is similar to that seen in previous studies of liquid metal–liquid silicate partitioning in a diamond anvil cell (Bouhifd and Jephcoat, 2003, 2011; Siebert et al., 2012, 2013), consisting of a spherical blob of metallic melt a few micrometers in diameter surrounded by silicate melt. Both the metal and silicate melts exhibit quench textures in all experiments (Fig. 2), also consistent with previous studies (Siebert et al., 2012, 2013). Quench texture in the metal consists of small (<100 nm) spherical blobs, rich in Si and O, though they are too small to determine whether or not they contain iron. Quench features in the silicate consist of small metallic blobs, rich in siderophile elements (Ni and Co). They are interpreted as quench features on the basis of morphology (they are small and regularly spaced) and composition (they have a very different composition from the central metallic melt, which is considered to have equilibrated with the silicate melt). We find no detectable compositional gradients within either the metallic or silicate melts.

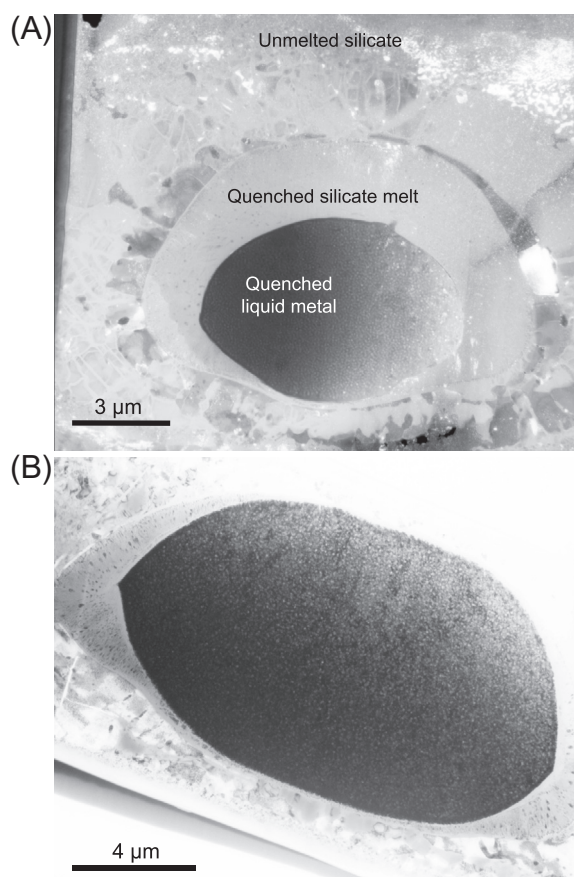


Fig. 2. TEM images of two of our recovered diamond cell experiments. (A) Sample recovered from 57 GPa and 4440 K, dark field image. (B) Sample recovered from 100 GPa and 5700 K, bright field image.

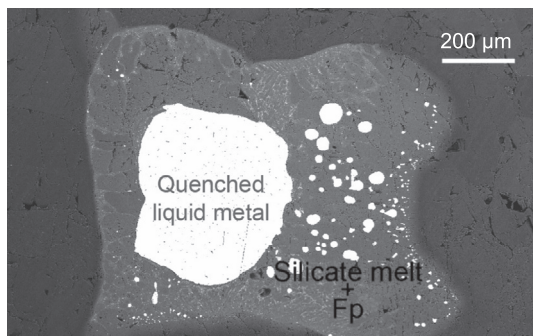


Fig. 3. Backscattered electron image of a recovered multianvil press sample from 25 GPa and 2850 K, run for 5 min. Fp, ferropericlase.

We sometimes, but not always, detect low abundances of Mg by TEM-EDX when analyzing metallic regions of diamond cell samples. Its abundance does not vary systematically with pressure or temperature, so we attribute it to spurious X-rays from the surrounding silicate, given the small sample sizes (Wade and Wood, 2012). This prevents an accurate measurement of Mg partitioning. Analyses of metal apparently containing less than 1 mol% Mg were corrected by subtracting a component of silicate melt to produce zero magnesium in the metal; analyses containing more Mg than this were not used in further calculations. In calculating the sample compositions, we also do not include small amounts of Pt or Cu (caused by spurious X-rays from the TEM grid) or Ga (implantation from the FIB process) detected by EDX.

A scanning electron image of one of our multianvil press run products is shown in Fig. 3. Their morphology is similar to that of previous multianvil press experiments on molten metal–silicate mixtures (e.g., Mann et al., 2009) and also the present diamond cell experiments, albeit at a much larger spatial scale. One or a few large metallic ponds (a few hundred micrometers across) were surrounded by silicate melt. In addition, ferropericlase coexisted as the liquidus phase. Quench textures in the metal consist of blobs several to ten micrometers across containing FeO and sometimes SiO₂, and/or needle and diamond-shaped inclusions of SiO₂ that are homogeneously distributed in a metal matrix (Fig. 3). In every experiment the metallic matrix was chemically homogeneous on the scale of electron microprobe analyses. These textures are similar to those of previous multianvil experiments in the Fe–Si–O system (e.g., O'Neill et al., 1998; Kawazoe and Ohtani, 2006). Quenched silicate melts exhibit elongated crystals of silicates (e.g., bridgmanite at 25 GPa). While large ferropericlase crystals formed in the silicate melt matrix, we found no systematic variation of the quenched silicate melt compositions over the whole area inside the capsule.

4. DISCUSSION

The 20 experiments presented here illustrate the partitioning behaviors of Ni, Co, V, Cr, Si, and O over a wide range of P – T conditions. When combined with literature

data (Table A.3), the effects of pressure, temperature, and composition on the partitioning behaviors of these elements can be modeled, and then applied to understanding the conditions of core formation and the composition of the Earth's core. In this section, we quantify partitioning in our experiments, parameterize compositional effects on the data, and model Earth's core formation.

4.1. Quantification of partitioning behavior

The metal–silicate partitioning behavior of an element M with valence n can be described by its partition coefficient,

$$D = \frac{X_M^{\text{met}}}{X_{\text{MO}_{n/2}}^{\text{sil}}}, \text{ where } X_M^{\text{met}} \text{ is the mole fraction of the element in}$$

the metallic melt and $X_{\text{MO}_{n/2}}^{\text{sil}}$ is the mole fraction of the element's oxide in the silicate melt. If n is known, the effects of oxygen fugacity can be removed through use of the exchange coefficient, which is defined as $K_D = D_M/D_{\text{Fe}}^{n/2}$. In the case of oxygen, the exchange coefficient is defined as $K_D = \frac{X_{\text{Fe}}^{\text{met}} X_{\text{O}}^{\text{met}}}{X_{\text{Fe}}^{\text{sil}} X_{\text{O}}^{\text{sil}}}$ (Frost et al., 2010). We have calculated D and K_D for each element that is present in both the metal and silicate melts in our experiments. The valence states of Cr and V in the silicate melt at high pressures are taken to be +2 and +3, respectively, based on previous studies (Corgne et al., 2008; Mann et al., 2009; Siebert et al., 2011). The values we found for D and K_D in each experiment are listed in Table 1. In the discussion below, we parameterize the effects of pressure and temperature on the partitioning of element i using the relationship:

$$\log_{10}(K_D^i) = a_i + \frac{b_i}{T} + \frac{c_i P}{T} \quad (2)$$

with pressure in GPa and temperature in Kelvin. This equation includes no compositional dependences, which will be discussed further in Section 4.2.

Two of our diamond cell experiments were run at nearly identical conditions, with differing silicon concentrations in the metallic starting materials. They were found to have similar final compositions, although one contained more carbon (Table A.2). The $\log K_D$ values for these two experiments are compatible within 2σ (Table 1), demonstrating that pressure and temperature have more control over partitioning than composition does. Several sets of multianvil press experiments were run at the same P – T conditions and varying oxygen fugacity (e.g., 25 GPa and 2950 K). The $\log K_D$ values that we calculated in these experiments are compatible within 2σ .

4.1.1. Partitioning of Ni and Co

The metal–silicate partitioning behaviors of Ni and Co are perhaps the best-studied of any siderophile elements at high P – T conditions (e.g., Fig. 4, caption), and are commonly used to infer conditions of core formation (Section 4.3.1). Fig. 4 is a compilation of many of the previous results on Ni and Co (Table A.3), along with our data from Table 1. The K_D values shown here have been recalculated from the original data of these studies to ensure a common definition. Not all of these studies focused on Ni and Co partitioning, but they all included these elements

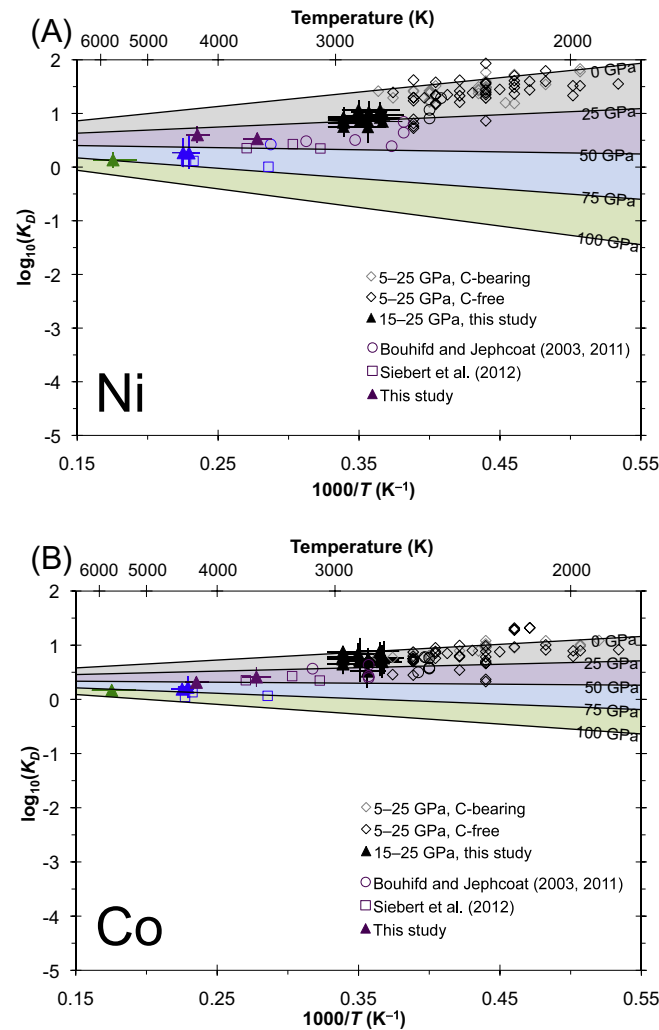


Fig. 4. Exchange coefficients of Ni (A) and Co (B). Uncorrected data (symbols) are shown compared to isobars calculated from the fits of Eq. (2) (Table 2), illustrating the temperature dependence of partitioning at fixed pressures. Error bars are shown only for the data from the present study (triangles). Data from $P > 25$ GPa are color-coded by pressure range (purple: 25–50 GPa, blue: 50–75 GPa, green: 75–100 GPa) with the symbol indicating the study. Data from 5 to 25 GPa are taken from Bouhifd and Jephcoat (2003), Bouhifd et al. (2013), Chabot et al. (2005), Corgne et al. (2008), Geßmann and Rubie (1998), Hillgren et al. (1996), Jana and Walker (1997), Kegler et al. (2008), Siebert et al. (2011), Thibault and Walter (1995), and this study. Only data without sulfur in the system are shown. Residuals are shown in Fig. A.1. (For interpretation of the references to color in this figure legend, the reader is referred to the web version of this article.)

in their experiments, allowing K_D to be calculated from their reported data. This figure highlights the relative lack of partitioning data at $P > 25$ GPa, despite the fact that core formation is thought to have occurred at higher effective pressures than this (e.g., Li and Agee, 2001; Bouhifd and Jephcoat, 2003, 2011; Wade and Wood, 2005; Kegler et al., 2008; Mann et al., 2009; Richter et al., 2011; Siebert et al., 2012), and this dearth of data at higher pressures makes it difficult to interpret partitioning data as a signature of core formation (Walter and Cottrell, 2013). This study aims to alleviate this problem by adding results from five experiments run at these higher pressure conditions.

In all of our figures and fitting, we do not use data with sulfur in the system. We also do not use data obtained from below 5 GPa, due to a possible change in the silicate melt

and/or metallic melt structure around this pressure that may affect partitioning (e.g., Kegler et al., 2008; Palme et al., 2011; Sanloup et al., 2011). The exclusion of data from below 5 GPa results in significantly better fits to our high pressure diamond anvil cell results. For completion, data from below 5 GPa are included in the compilation of literature data in Table A.3 (e.g., Chabot and Agee, 2003; Richter et al., 2010).

In the case of both nickel and cobalt, the data from our two experiments at nearly identical conditions but different carbon contents (blue triangles) are indistinguishable. Additionally, comparing carbon contents of the $P < 25$ GPa data shown in Fig. 4 does not reveal any systematic trends of partitioning with C content. Therefore, it is apparent from these data that carbon does not play a significant role in controlling the partitioning behaviors of

Ni and Co, at least at low carbon contents, which is consistent with previous results at high P – T (e.g., Chabot et al., 2005; Siebert et al., 2011).

We have fit Eq. (2) to all of the data from $P > 5$ GPa on Ni and Co partitioning, and the resulting parameters are listed in Table 2. Ni partitioning has a stronger pressure and temperature dependence than Co partitioning. The values of a , b , and c we find for Ni and Co (Table 2) fall within the broad range of values determined in previous studies, which are summarized in Siebert et al. (2012), and they agree within 2σ with the coefficients found by that study. We obtain good fits to the data using Eq. (2), with a root mean squared (rms) misfit to $\log K_D$ of 0.15 and 0.18 log units for Ni and Co, respectively.

Fig. 4 also shows isobars calculated from the fitted parameters given in Table 2. Good fits are obtained without any corrections for the light element content of the metal, illustrating the relative insensitivity of nickel and cobalt to the metallic melt composition. Fig. A.1 illustrates the residuals to the fits for Ni and Co. Our fits adequately describe the Ni and Co partitioning data of this study as well as those of the previous diamond anvil cell studies (Bouhifd and Jephcoat, 2003, 2011; Siebert et al., 2012). This broad agreement between these studies on the partitioning behaviors of Ni and Co is remarkable given the

complexity of experiments and analyses from these P – T conditions. Fig. A.2 is analogous to Fig. 4, but shows $\log K_D$ as a function of pressure.

At low pressures, both Ni and Co become less siderophile relative to iron (lower K_D) with increasing temperature. As pressure increases, their partitioning becomes less sensitive to temperature, and at ~ 45 GPa the temperature dependence reverses (Figs. 4 and A.2). At higher pressures, Ni and Co become more siderophile relative to iron with increasing temperature. This behavior is consistent with previous results on Ni and Co partitioning (Siebert et al., 2012) and with the relative behaviors of the Ni–NiO and Fe–FeO oxygen fugacity buffers at high P – T conditions, calculated from the equations of state of coexisting metal–oxide pairs, whose difference describes the ideal component of Ni partitioning (Campbell et al., 2009). Results of these previous studies on Ni partitioning are compared in Fig. A.3.

4.1.2. Partitioning of V and Cr

The partition coefficients of V and Cr are known to be sensitive to carbon content at $P < 25$ GPa (e.g., Mann et al., 2009; Siebert et al., 2011). Additionally, a recent study by Siebert et al. (2013) presents data on the partitioning of V and Cr with a discontinuous increase in $\log K_D$ of

Table 2

Parameterizations of partitioning data from Eq. (2). Uncertainties do not account for covariance between terms. Variance–covariance matrices describing the Ni, Co, Si, and O fits are shown in Tables A.5–A.8.

| Element i | a_i | b_i (K) | c_i (K/GPa) | R^2 | rms $\log K_D$ | # data | # studies | Studies |
|-------------|-----------------|-------------------|---------------|-------|----------------|--------|-----------|---|
| Ni | 0.46 ± 0.16 | 2700 ± 300 | -61 ± 6 | 0.89 | 0.15 | 109 | 13 | Bouhifd and Jephcoat (2003, 2011), Bouhifd et al. (2013), Chabot et al. (2005), Corgne et al. (2008), Geßmann and Rubie (1998), Hillgren et al. (1996), Jana and Walker (1997), Kegler et al. (2008), Siebert et al. (2011, 2012), Thibault and Walter (1995), this study |
| Co | 0.36 ± 0.15 | 1500 ± 300 | -33 ± 5 | 0.57 | 0.18 | 97 | 11 | Bouhifd and Jephcoat (2003, 2011), Chabot et al. (2005), Geßmann and Rubie (1998), Hillgren et al. (1996), Jana and Walker (1997), Kegler et al. (2008), Siebert et al. (2011, 2012), Thibault and Walter (1995), this study |
| V | -0.3 ± 0.6 | -5400 ± 1200 | 19 ± 19 | 0.66 | 0.33 | 42 | 6 | Geßmann and Rubie (1998), Mann et al. (2009), Siebert et al. (2011, 2013), Wade and Wood (2005), this study |
| Cr | 0.0 ± 0.3 | -2900 ± 700 | 9 ± 11 | 0.51 | 0.21 | 53 | 8 | Corgne et al. (2008), Geßmann and Rubie (1998), Mann et al. (2009), Siebert et al. (2011, 2013), Thibault and Walter (1995), Wade and Wood (2005), this study |
| Si | 1.3 ± 0.3 | $-13,500 \pm 900$ | | 0.76 | 0.43 | 64 | 8 | Bouhifd and Jephcoat (2011), Corgne et al. (2008), Geßmann and Rubie (1998), Ito et al. (1995), Mann et al. (2009), Siebert et al. (2012), Tsuno et al. (2013), this study |
| O | 0.6 ± 0.4 | -3800 ± 900 | 22 ± 14 | 0.52 | 0.29 | 79 | 10 | Bouhifd and Jephcoat (2011), Chabot et al. (2005), Corgne et al. (2008), Geßmann and Rubie (1998), Hillgren et al. (1996), Jana and Walker (1997), Ricolleau et al. (2011), Siebert et al. (2012), Tsuno et al. (2013), this study |

~ 1 log unit for V and ~ 0.5 log units for Cr at 25–30 GPa, which also corresponds to a change in apparatus from a multianvil press to a diamond anvil cell.

Fig. 5 summarizes the previous results on V and Cr from Siebert et al. (2013) and several multianvil press studies from S-free systems. The data below 25 GPa are color-coded as to whether or not they contain carbon, illustrating the strong effect that carbon has on the partitioning of these elements. Fig. 5 also shows our results on V and Cr. They are consistent with the recent results of Siebert et al. (2013), with both diamond anvil cell studies implying more siderophile behavior of V and Cr than would be expected by extrapolating the C-free data from lower pressures. This behavior can be understood through the effects of metallic melt composition or may indicate a change in valence, as discussed in Section 4.2.2. The parameters in

Table 2 describe the fits of Eq. (2) to V and Cr partitioning data from $P > 5$ GPa. Neither element has a resolvable pressure dependence. These fits are not as good as for Ni and Co, due to compositional effects on V and Cr partitioning and/or valence changes (Section 4.2.2), resulting in rms misfits to $\log K_D$ of 0.33 and 0.21 log units for V and Cr, respectively, with systematic offsets correlated with metallic melt composition.

4.1.3. Partitioning of Si and O

Si and O are thought to be at least partly responsible for the core's density deficit (e.g., Poirier, 1994; Allègre et al., 1995; McDonough, 2003), so a better understanding of their partitioning could help to clarify the light element composition of the Earth's core. In our experiments we have produced metallic compositions containing up to

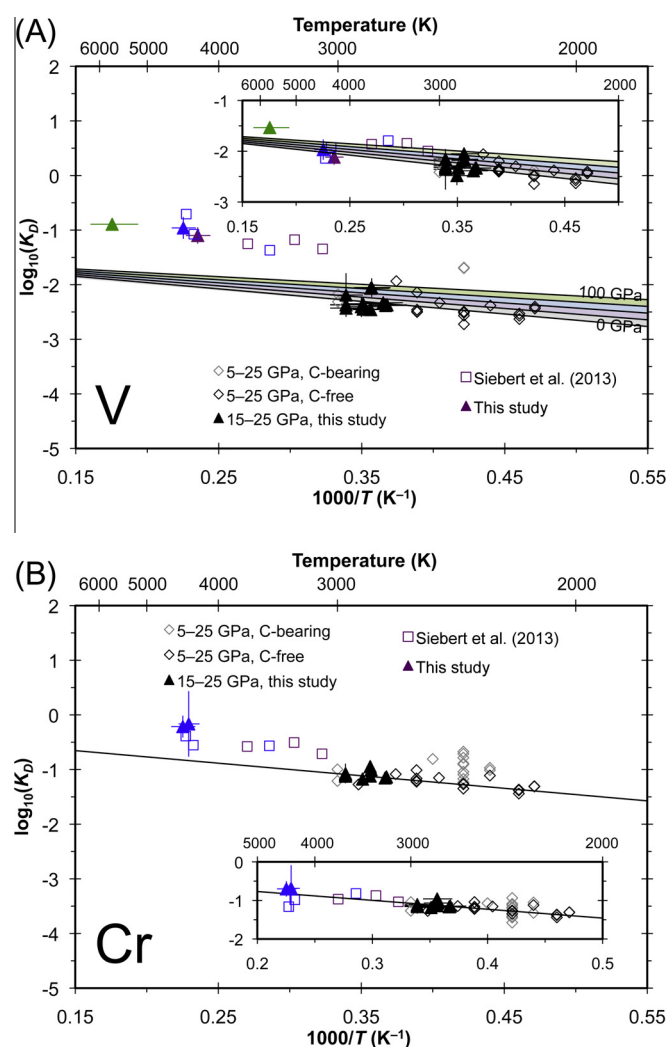


Fig. 5. Exchange coefficients of V (A) and Cr (B). Uncorrected data (symbols) are shown compared to isobars calculated from the fits of Eq. (3) (Table 3) corrected to no light elements (lines), illustrating the temperature dependence of partitioning at fixed pressures (the very small pressure dependence in the Cr fit is not shown). The insets show the data corrected for the presence of O, Si, and C. Only data from the present study (triangles) have error bars. Data from $P > 25$ GPa are color-coded by pressure range (purple: 25–50 GPa, blue: 50–75 GPa, green: 75–100 GPa) with the symbol indicating the study. Data from 5 to 25 GPa are taken from Corgne et al. (2008), Geßmann and Rubie (1998), Mann et al. (2009), Siebert et al. (2011), Thibault and Walter (1995), Wade and Wood (2005), and this study. Only data without sulfur in the system are shown. Residuals are shown in Fig. A.5. (For interpretation of the references to color in this figure legend, the reader is referred to the web version of this article.)

11.3 wt% O and 8.8 wt% Si (Table A.2), significantly more than the Earth's core could contain based on its density (e.g., Fischer et al., 2011, 2014). This implies that we have surpassed the mean conditions of core formation in our experiments, and we can now interpolate rather than extrapolate our metal–silicate partitioning data.

Fig. 6 shows previous results on Si and O partitioning from Siebert et al. (2012), Bouhifd and Jephcoat (2011), and various multianvil press studies, as well as the results of the present study. The Si and O data are both approximately linear in inverse temperature, suggesting minimal pressure dependence. Silicon partitioning has a stronger temperature dependence (steeper slope) than oxygen. We have fit Eq. (2) to the Si and O partitioning data from $P > 5$ GPa, and the resulting parameters are listed in Table 2. Fig. 6 illustrates fits to the data, with the residuals to these fits shown in Fig. A.4.

4.2. Epsilon modeling

To correct for compositional effects on the exchange coefficient K_D , we use the epsilon formalism of Ma (2001) to describe non-ideal interactions of N components in the Fe-rich liquid:

$$\log_{10} K_D^i = a_i + \frac{b_i}{T} + \frac{c_i P}{T} + \frac{e_i^j \ln(1 - X_i)}{2.303} + \frac{1}{2.303} \sum_{k=2}^N e_k^j X_k \left(1 + \frac{\ln(1 - X_k)}{X_k} - \frac{1}{1 - X_i} \right) - \frac{1}{2.303} \sum_{k=2}^N e_k^j X_k^2 X_i \left(\frac{1}{1 - X_i} + \frac{1}{1 - X_k} + \frac{X_i}{2(1 - X_i)^2} - 1 \right) \quad (3)$$

where X_i is the mole fraction of component i in the liquid (here $i = 1$ for Fe), $e_i^k = e_k^i$ is the interaction parameter of elements i and k in the liquid, and the factor of 2.303

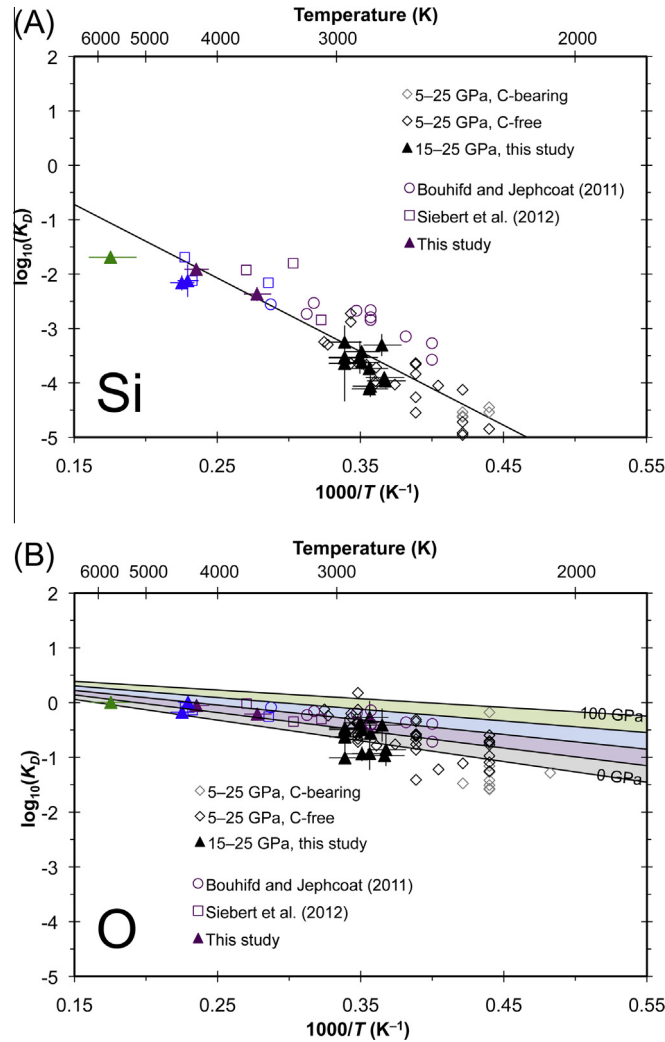


Fig. 6. Exchange coefficients of Si (A) and O (B). Uncorrected data (symbols) are shown compared to the fits of Eq. (2) (Table 2). Partitioning of Si has no resolvable pressure dependence. Only data from the present study (triangles) have error bars. Data from $P > 25$ GPa are color-coded by pressure range (purple: 25–50 GPa, blue: 50–75 GPa, green: 75–100 GPa) with the symbol indicating the study. Data from 5 to 25 GPa are taken from Chabot et al. (2005), Corgne et al. (2008), Geßmann and Rubie (1998), Hillgren et al. (1996), Ito et al. (1995), Jana and Walker (1997), Mann et al. (2009), Ricolleau et al. (2011), Tsuno et al. (2013), and this study. Only data without sulfur in the system are shown. Residuals are shown in Fig. A.4. (For interpretation of the references to color in this figure legend, the reader is referred to the web version of this article.)

converts natural logarithms to base-10 logarithms. Terms involving epsilons describe the compositional effects of the metallic liquid on the activity coefficient of element i . In writing this equation, we assume that the ratio $\gamma_{\text{MO}_{n/2}}/\gamma_{\text{FeO}}^{n/2}$ (where γ is an activity coefficient) is not a strong function of silicate melt composition, after [Wade and Wood \(2005\)](#). We do not include any explicit dependence on silicate melt composition, because no resolvable effect was found in this dataset. It is also assumed here that the activity coefficient of Fe in the metal (γ_{Fe}) is not dependent on composition over the compositional range studied. This term, along with a γ_i^0 term ([Ma, 2001](#)), are not explicitly included in Eq. (3) because they both follow an $a + b/T + cP/T$ dependence, and so they are incorporated into the a_i , b_i , and c_i fitting parameters.

For each element of interest ($i = \text{Ni, Co, V, Cr, Si, O}$), the parameters a_i , b_i , and c_i are fit, as well as various interaction parameters. Self-interaction parameters (e_i^i) are assumed to be negligible for trace metals (Ni, Co, V, and Cr), but not for light elements (Si, O, and C). We do not fit interactions between trace metals, whose abundances are too low to have a significant effect on each other. We consider interaction parameters between each trace element and each of the three light elements. The parameter e_k^i at temperature T is described in the *Steelmaking Data Sourcebook* ([Japan Society for the Promotion of Science and the Nineteenth Committee on Steelmaking, 1988](#)) as

$$e_k^i(T) = \frac{e_k^i M_i T_{\text{ref}}}{0.242} \frac{1}{T} - \frac{M_i}{55.85} + 1 \quad (4)$$

where M_i is the molar mass of element i (in g/mol) and T_{ref} is the reference temperature at which the interaction parameter e_k^i is determined. We fit a_i , b_i , c_i , e_{O}^i , e_{Si}^i , and e_{C}^i for each element, using $T_{\text{ref}} = 1873$ K as in the steelmaking literature. The results are shown in [Table 3](#). No pressure dependence on the epsilon terms was resolvable at the 95% confidence level. These parameters quantify the effects of light elements on the partitioning of other elements in the system.

4.2.1. Compositional effects on nickel and cobalt partitioning

Nickel and cobalt are highly insensitive to metallic melt composition, and are fit well without compositional terms. Fitting Eq. (3) to the Ni and Co data resulted in no epsilon terms that were significant at the 95% confidence level. [Table A.4](#) lists epsilon values for Ni and Co published in the *Steelmaking Data Sourcebook* ([Japan Society for the Promotion of Science and the Nineteenth Committee on](#)

[Steelmaking, 1988](#)) and [Tuff et al. \(2011\)](#). Most of the values in the *Steelmaking Data Sourcebook* are non-zero but small, in general agreement with our findings. [Tuff et al. \(2011\)](#) report significantly larger values of $e_{\text{Si}}^{\text{Ni}}$ and $e_{\text{Si}}^{\text{Co}}$, which are inconsistent with our more extensive dataset.

4.2.2. Compositional effects on vanadium and chromium partitioning

In contrast to nickel and cobalt, V and Cr partitioning are strongly dependent on the metallic melt composition in our analysis. The isobars shown in [Fig. 5](#) are calculated from the fitted parameters in [Table 3](#), extrapolated to zero light elements in the metal. For vanadium and chromium, only the data below 25 GPa without C were not strongly affected by the presence of light elements in the metallic melt ([Fig. 5](#)). The insets in [Fig. 5](#) illustrate the fits to the data after correction to no light elements. Pressure has a very weak effect on the partitioning of Cr, with its P/T coefficient indistinguishable from zero ([Table 3](#)). The parameter $e_{\text{Si}}^{\text{Cr}}$ is also not significant at the 95% confidence level. [Fig. A.5](#) illustrates the residuals to the fits for V and Cr. Adding compositional terms significantly improves the fits to V and Cr partitioning data, lowering the rms misfits on $\log K_D$ to 0.14 and 0.13, respectively ([Table 3](#)).

The strong effect of carbon on V and Cr partitioning is evident from a comparison of the multianvil press data with and without carbon; however, it cannot explain the increased siderophility observed at higher pressures. Even with our ability in this study to accurately measure carbon in the metallic melt using EELS, we find too small an amount to account for this behavior. One explanation for this increased siderophility is the interaction of oxygen with V and Cr as first proposed by [Siebert et al. \(2013\)](#) and described here by the parameters in [Table 3](#). The apparent discontinuity in the siderophility of these elements is due to the much higher oxygen contents of the metallic melts in diamond cell experiments. It can be entirely corrected using the epsilon formalism ([Fig. 5](#) insets), though this results in a very large correction due to oxygen of up to >1 log unit for V and >0.5 log units for Cr. This change in K_D at high pressures could also be due to an increase in the valence states of these elements in the silicate melts instead of being a consequence of strong interactions with oxygen in the metal. A change in valence could be induced by the higher pressures and temperatures in diamond anvil cell experiments, similar to the possible pressure-induced valence change in tungsten in silicate melts ([Cottrell et al., 2009](#)), or by the higher $f\text{O}_2$ in these experiments. Applying Eq. (1) to the compositions from previous studies reported in [Table A.3](#) shows that

Table 3

Results of epsilon modeling. Parameters for each element were fitted to Eqs. (3) and (4), where e_k^i is fit at 1873 K. The same data were fit as in [Table 2](#). Uncertainties do not account for covariance between terms. Variance–covariance matrices describing the V and Cr fits are shown in [Tables A.9 and A.10](#).

| Element i | e_{O}^i | e_{Si}^i | e_{C}^i | a_i | b_i (K) | c_i (K/GPa) | R^2 | rms $\log K_D$ |
|-------------|--------------------|-------------------|--------------------|----------------|-------------------|---------------|-------|----------------|
| V | -0.077 ± 0.008 | 0.039 ± 0.014 | -0.036 ± 0.005 | -1.5 ± 0.3 | -2300 ± 700 | 9 ± 9 | 0.94 | 0.14 |
| Cr | -0.037 ± 0.007 | | -0.015 ± 0.002 | -0.3 ± 0.2 | -2200 ± 600 | -5 ± 7 | 0.81 | 0.13 |
| Si | -0.06 ± 0.02 | | | 0.6 ± 0.3 | $-11,700 \pm 800$ | | 0.82 | 0.37 |
| O | -0.12 ± 0.04 | -0.11 ± 0.05 | 0.11 ± 0.02 | 0.1 ± 0.4 | -2200 ± 900 | 5 ± 12 | 0.67 | 0.24 |

these diamond anvil cell experiments on V and Cr partitioning span IW–0.6 to IW–1.4, while these multianvil press experiments on their partitioning span IW–1.4 to IW–5.2; these two types of experiments do not overlap in pressure or oxygen fugacity, so caution should be used when interpreting discontinuities between them. Previous work at pressures up to 18 GPa are consistent with valence states of +2 for Cr and +3 for V (Corgne et al., 2008; Mann et al., 2009; Siebert et al., 2011), so there is no direct support for this interpretation. Future work on the valences of V and Cr in silicate melts at pressures extending beyond 30 GPa and at a greater range of fO_2 could help resolve this issue.

Table A.4 compares the epsilon values we found for V and Cr to those reported in the *Steelmaking Data Sourcebook* (Japan Society for the Promotion of Science and the Nineteenth Committee on Steelmaking, 1988), Tuff et al. (2011), and Siebert et al. (2013). The values found in this study generally agree with previous results within mutual 2σ uncertainty. For example, this study and Siebert et al. (2013) found values for ϵ_{Si}^{Cr} of -7.9 ± 1.6 and -7.2 ± 2.1 , respectively. The largest disagreement is reported for ϵ_{Si}^V (8 ± 3 in this study, 2.0 ± 0.4 in Tuff et al. (2011), and 5.2 in the *Steelmaking Data Sourcebook*). Some of the observed discrepancies may indicate that dependences on different light elements are correlated. For example, experiments at higher pressures and temperatures tend to contain both increased Si and O concentrations in the metal, making it difficult to accurately distinguish their effects. The results of the present study are based on data obtained over a wide range of pressure (5–100 GPa) and temperature (up to 5700 K), while previous studies are based only on 1 bar data or data from a more limited P – T range, which may influence the results. The inclusion of data from $P < 5$ GPa in previous studies may also account for some of this variation.

4.2.3. Compositional effects on silicon and oxygen partitioning

Fig. A.6 illustrates our fits of Eq. (3) to the partitioning data of Si and O. The insets demonstrate a closer correspondence after correcting the data to infinitesimal light element concentrations. We find no resolvable pressure effects on Si partitioning. The Si–Si and Si–C interaction parameters e_{Si}^{Si} and e_C^{Si} are also not significant at the 95% confidence level, so they were held fixed at zero in the fits.

We find values of Si–O and O–O interaction parameters that produce positive interactions during the partitioning of these elements, in agreement with the findings of Tsuno et al. (2013). For example, higher oxygen contents in the metal will cause more oxygen and more silicon to partition into the metal. The epsilon fits describe the partitioning data, but are not stable for use in modeling the composition of the Earth's core (Section 4.3) due to this runaway effect, which causes models to become unstable at high light element contents of the metal. This problem points to the need for additional partitioning data at high pressures and temperatures from diamond anvil cell experiments.

Interactions involving Si and O in metallic melts have been investigated in several previous studies (e.g., Japan

Society for the Promotion of Science and the Nineteenth Committee on Steelmaking, 1988; Dresler, 1989; Bouchard and Bale, 1995; Shibaev and Grigorovich, 2008; Ricolleau et al., 2011; Tuff et al., 2011; Tsuno et al., 2013). The epsilon values ϵ_{Si}^{Si} , ϵ_O^{Si} , ϵ_C^{Si} , ϵ_O^O , and ϵ_C^O from these studies are compared to our results in Table A.4. The epsilon values from different studies disagree in some cases, possibly due to correlations in light element contents or other pressure or temperature effects (Section 4.2.2).

4.3. Applications of partitioning data

Matching the observed mantle composition of Ni and Co using high P – T partitioning can offer insight into the conditions of core formation and/or the composition of the Earth's core. In this section, we use geochemical constraints on the core and mantle compositions to model core formation at a single effective pressure and temperature and under evolving P – T – fO_2 conditions.

4.3.1. Core formation at a single effective pressure and temperature

Many previous studies have used Ni and Co partitioning to determine a single pressure and temperature of core formation (e.g., Li and Agee, 1996, 2001; Wade and Wood, 2005; Siebert et al., 2011, 2012); here we reproduce this calculation using our new results. Though core formation likely occurred in a series of stages as the Earth grew (Section 4.3.2), consideration of a single pressure–temperature equilibration can provide a useful shorthand for the complex history of the planet. It can be thought of as the effective conditions of core formation, allowing for calculation of the core's composition and comparisons between partitioning results.

Many studies (e.g., McDonough and Sun, 1995; Allègre et al., 1995; McDonough, 2003) have reported compositions of the bulk silicate Earth and the core. Adopting the compositions from McDonough (2003) and McDonough and Sun (1995) and constraining core formation to occur along the mantle liquidus of Andraut et al. (2011), we use our parameterizations of Ni and Co partitioning (Table 2) to calculate a P – T point for both Ni and Co that reproduces the Earth's effective exchange coefficients. To produce nickel's effective $\log K_D$ of 0.30 and cobalt's $\log K_D$ of 0.26 (at an fO_2 of IW–2) requires partitioning at 54 ± 5 GPa and the corresponding liquidus temperature of 3300–3400 K (Andraut et al., 2011). The partitioning behaviors of both elements point to the same P – T conditions, which is important agreement given uncertainties in the core composition, the parameterization of the data, and the liquidus of the mantle. Fig. 7 illustrates these findings, mapping out the regions of P – T space that can reproduce the Earth's distributions of Ni and Co. Constraining core–mantle equilibration to instead occur between the mantle's solidus and liquidus (Andraut et al., 2011) leads to a core formation pressure of 46–57 GPa and temperature of 2800–3400 K. These results are in good agreement with the findings of Bouhifd and Jephcoat (2011) and Siebert et al. (2012), and are higher than results of earlier studies that did not benefit from data above 25 GPa (e.g., Li and

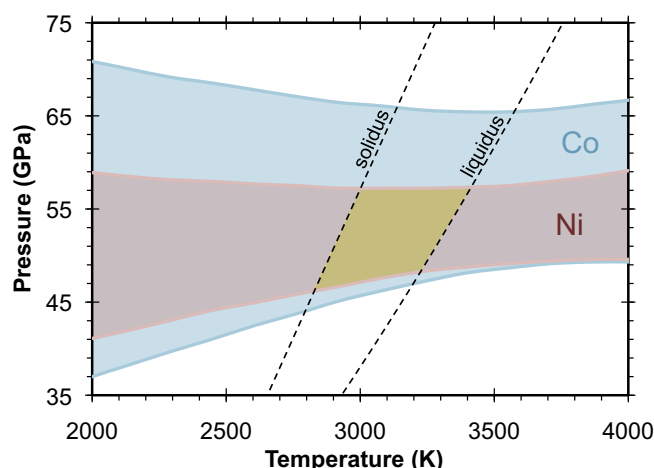


Fig. 7. Pressure–temperature conditions of single-stage core formation, constrained by Ni and Co partitioning. Pink and blue shaded regions: P – T conditions that produce the Earth's K_D of Ni and Co, respectively. Dashed black lines: solidus and liquidus of the mantle (Andraut et al., 2011). Yellow shaded region: solution space of P – T conditions that simultaneously reproduce the Earth's Ni and Co distributions at the base of a magma ocean. Calculation is done at an oxygen fugacity of IW–2. This model suggests core formation at 46–57 GPa. (For interpretation of the references to color in this figure legend, the reader is referred to the web version of this article.)

Agee, 1996). The widths of the shaded regions in Fig. 7 are calculated by propagating the variance–covariance matrices of the Ni and Co fits (Tables A.5 and A.6) through the calculation.

We can then use this effective pressure and temperature of core–mantle equilibration to predict the core's light element concentration, which is independently constrained by equation of state measurements. Comparing the densities of FeO, Fe–Si alloys, and pure Fe at core conditions to the seismologically-determined density of the core allows for calculation of the amount of each light element needed to reproduce the core's density deficit. The outer core's density can be matched by the addition of 11 wt% Si or 8 wt% O to an Fe–Ni alloy for a core–mantle boundary temperature of 4000 K (Fischer et al., 2011, 2014), making these the maximum amounts of these elements that can be present in the core. Using our new parameterizations (Table 2), we find that equilibration at 54 ± 5 GPa and 3350 ± 50 K would produce a core containing 8.5 ± 1.4 wt% Si and 1.6 ± 0.3 wt% O (uncertainties calculated from the variance–covariance matrices describing the Si and O fits, Tables A.7 and A.8), in agreement with the modeling of Rubie et al. (2015a). A core of this composition is broadly consistent with the core's measured density, based on equation of state measurements (Fischer et al., 2011, 2014). Therefore the partitioning behaviors of Ni, Co, Si, and O are all compatible with a single-stage model of core formation at an effective pressure and temperature of 54 GPa and 3350 K. The presence of other elements in the core, especially S, could further influence the partitioning of Si and O. Additional experiments on metal–silicate partitioning in the presence of sulfur are needed to clarify its effects.

Our epsilon modeling on V and Cr can be used to calculate their distributions in the Earth. Single-stage partitioning at 54 GPa and 3350 K with 8.5 wt% Si and 1.6 wt% O in the metal would yield partition coefficients (D) of

0.37 ± 0.07 for V and 1.7 ± 0.3 for Cr (uncertainties calculated from the variance–covariance matrices describing the V and Cr fits, Tables A.9 and A.10). These values are lower than their apparent values in the Earth of 2 and 3.5, respectively, according to McDonough (2003) and McDonough and Sun (1995). This result is consistent with the findings of Wade and Wood (2005) that the partition coefficients of Ni, Co, and V cannot be simultaneously reproduced along the mantle liquidus at a fixed oxygen fugacity. The broader ranges of possible partition coefficients for the bulk Earth reported by Wood et al. (2006) (1.5–2.2 for D_V and 0.5–3.5 for D_{Cr}) suggest that we cannot rule out the possibility of reproducing the partition coefficient of Cr in a single stage model of core formation, but that of V is still difficult to match.

4.3.2. Core formation over a range of pressures and temperatures

As an improvement upon the single-stage model described above (Section 4.3.1), we can apply our results to models of core formation over a range of pressures and temperatures, since core formation is thought to have actually occurred in a series of equilibration steps during Earth's accretion. We have performed modeling similar to that in many previous partitioning studies (e.g., Wade and Wood, 2005; Wood et al., 2009; Ricolleau et al., 2011; Siebert et al., 2011, 2012, 2013; Wade et al., 2012), in which the Earth is built through the accretion of twenty 0.05 Earth mass planetary embryos. Each embryo is assigned an initial metal and silicate composition and metal fraction (Table A.11). With each collision, the impactor's metal and silicate equilibrate at 2/3 of the growing Earth's core–mantle boundary pressure (Rubie et al., 2011) and the liquidus temperature at that pressure (Andraut et al., 2011), then its metal and silicate are added to the Earth's core and mantle. Partitioning is determined

using our parameterizations for Ni, Co, Si, and O from Table 2, and our parameterizations using the epsilon formalism for V and Cr from Table 3.

Unlike previous partitioning studies that include models of incremental core formation by imposing a fixed or changing oxygen fugacity (e.g., Wade and Wood, 2005; Wood et al., 2009; Ricolleau et al., 2011; Siebert et al., 2011, 2012, 2013; Wade et al., 2012), we follow the methodology of Rubie et al. (2011) in allowing oxygen fugacity to evolve self-consistently as the Earth grows from impactors of specified compositions. The Fe, Si, and Ni contents of the mantle and Fe, Si, Ni, and O contents of the core are calculated simultaneously from a system of seven equations (mass balances for each of these four elements and partitioning parameterizations for Si, Ni, and O), then trace element partitioning is calculated. The oxygen fugacity relative to the IW buffer (or equivalently, the FeO content of the mantle and Fe content of the core) is a result of the equilibration calculation, not an input. If an oxygen fugacity

relative to IW were to be imposed, the partitioning behavior of either silicon or oxygen would be specified by that oxygen fugacity instead of constrained by experimental data. Otherwise, there would be a violation of mass balance, because any change in the iron distribution (caused by imposing an oxygen fugacity) must be compensated by a change in the silicon distribution to avoid creating or destroying oxygen atoms.

We tested four different distributions of initial compositions in our modeling. The two starting compositions, which were generated by equilibrating a bulk composition similar to a CI chondrite at two different oxygen fugacities, are listed in Table A.11. Results are shown in Fig. 8. We found the best fit to the Earth's trace element distributions by either building the Earth from a more reduced composition (IW–3.5), or by assigning the first 75% of incoming material a more reduced composition and the final 25% a more oxidized composition (IW–1.5) (Fig. 8B). The case of increasing oxidation state of incoming material with time

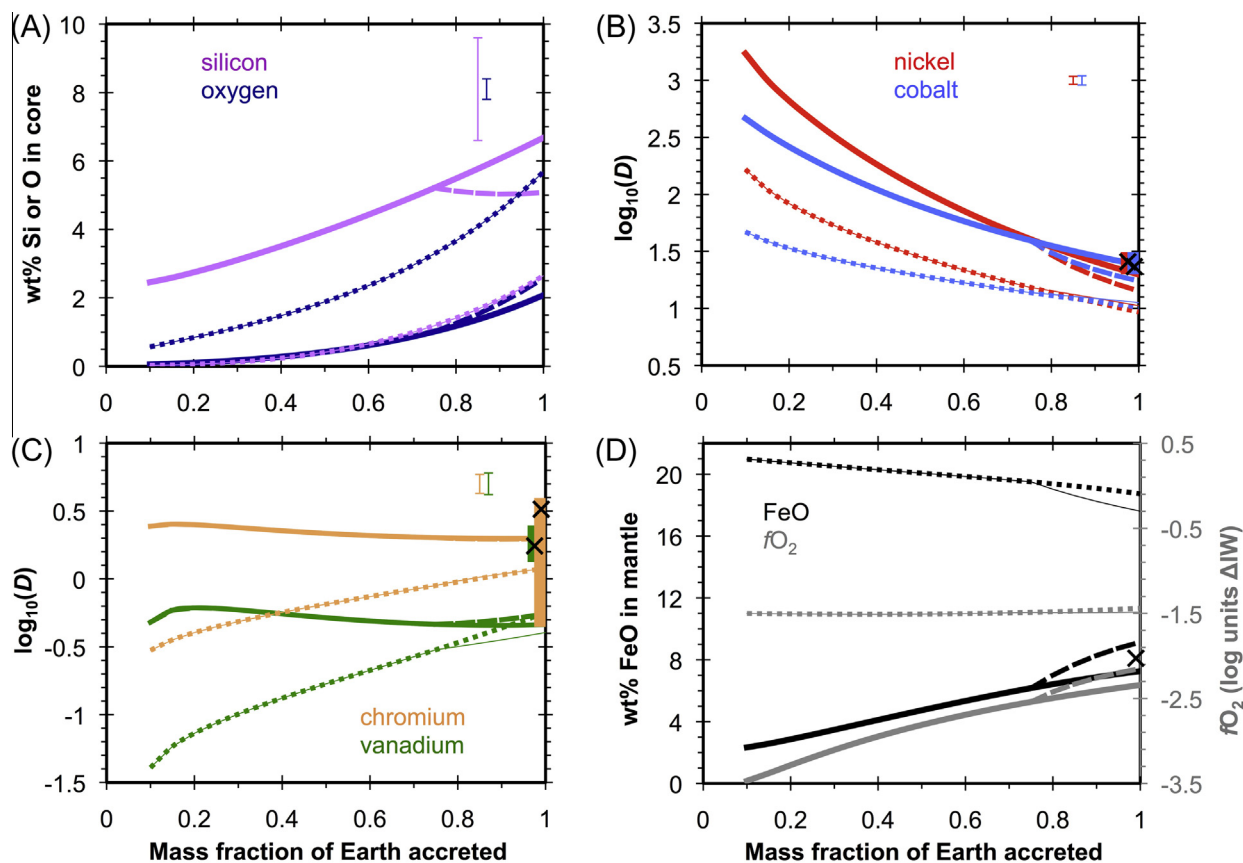


Fig. 8. Results of modeling of Earth's core formation taking place over a range of pressures and temperatures. (A) Light element composition of the core (silicon: purple, oxygen: blue) throughout Earth's accretion. (B) Log of core–mantle partition coefficients of nickel (red) and cobalt (blue). (C) Log of core–mantle partition coefficients of chromium (orange) and vanadium (green). (D) FeO in the mantle (black, left axis) and bulk planetary oxygen fugacity relative to the IW buffer (grey, right axis). Filled rectangles are Earth values from Wood et al. (2006), black \times symbols are Earth values from McDonough (2003) (parts B–D). Thick solid lines: model in which Earth is built from reduced materials (IW–3.5). Dotted lines: model in which Earth is built from more oxidized materials (IW–1.5). Dashed lines: model in which Earth is built from reduced materials for the first 75% of accretion, then built from oxidized materials. Thin solid lines: model in which Earth is built from oxidized materials for the first 75% of accretion, then built from reduced materials. Representative error bars (calculated for the reduced model from the variance–covariance matrices of the partitioning data fits, Tables A.5–A.10) are shown in parts A–C. (For interpretation of the references to color in this figure legend, the reader is referred to the web version of this article.)

has been shown to best reproduce the Earth's composition with regard to many elements (Rubie et al., 2011, 2015a), and it is compatible with *N*-body simulations of terrestrial planet formation, which show that the Earth tends to accrete material from farther from the Sun (more oxidized material) at later times (e.g., Raymond et al., 2006; Fischer and Ciesla, 2014; Rubie et al., 2015a). Fig. 8 also shows a case in which the Earth is built entirely from the more oxidized composition, which does not reproduce most trace element distributions as well. We tested a case in which the first 75% of the Earth was built from oxidized material and the last 25% from reduced material, inspired by the model of Siebert et al. (2013); the results were virtually indistinguishable from the oxidized case. This finding is consistent with the recent study of Rubie et al. (2015a), who also failed to produce a good fit to Earth's composition through the accretion of more reduced material at later times. Fig. 8D shows that the incorporation of more reduced material at later times is unable to lower the initially high FeO content of the mantle when Si partitioning is included because we use a self-consistent mass balance calculation for oxygen, whereas the FeO content of the mantle can be approximately reproduced when starting with more reduced materials.

Our models do not match Earth's vanadium distribution as well as they match those of other trace elements (Fig. 8C). The more oxidized model provides a better match for vanadium by increasing its *D* value at high pressures, but this counterintuitive result is an artifact of a large V–O interaction in the epsilon model. Vanadium's partitioning behavior at high pressures may be better explained by a change in its valence state in the silicate melt (Section 4.2.2). Alternatively, V and Cr may be preferentially hosted in deep mantle phases. If so, their apparent partition coefficients in the Earth, calculated from measurements of upper mantle composition, are not accurate (Righter, 2011, 2015). Previous studies in the piston-cylinder apparatus and multianvil press (Chabot and Agee, 2003; Mann et al., 2009; Siebert et al., 2011; Wood et al., 2014) have shown that both C and S make vanadium more siderophile, which would provide a better match to Earth's apparent *D* if these elements are present in the core.

The presently-available partitioning data can be used to match the Earth's Cr distribution in any of the models we tested when comparing to the very broad range of possible Earth compositions from Wood et al. (2006) (Fig. 8C), while none of the models are a good match to the V distribution, though this could be explained by a change in V valence, preferential hosting in lower mantle minerals, or interactions with C or S, as discussed above. Based on these complications, these elements may not presently be good candidates for discriminating between models for Earth's formation with different oxidation states (e.g., Siebert et al., 2013). Further work on the partitioning of vanadium in a diamond anvil cell, especially quantification of its valence state, the effects of sulfur and carbon, and partitioning between different mantle phases, will help clarify this issue.

Fig. 8A shows the evolution of the core's silicon and oxygen contents. For the cases of reduced building blocks

or reduced then oxidized building blocks, the Earth's core is predicted to contain more silicon than oxygen, but substantial quantities of both (2.1–2.6 wt% O and 5.1–6.7 wt% Si). For the case of oxidized building blocks, the situation is reversed. In each case, our models produce core compositions that are broadly consistent with the amounts of light elements needed to match the core's density according to most previous studies (e.g., Sata et al., 2010; Fischer et al., 2011, 2014; Zhang et al., 2014).

5. CONCLUSIONS

The metal–silicate partitioning of Ni, Co, V, Cr, Si, and O have been measured in 15 multianvil press experiments and five diamond anvil cell experiments up to 100 GPa and 5700 K. These new data were combined with literature data from 18 previous studies for a total of 179 experiments (Ito et al., 1995; Thibault and Walter, 1995; Hillgren et al., 1996; Jana and Walker, 1997; Geßmann and Rubie, 1998; Bouhifd and Jephcoat, 2003, 2011; Chabot et al., 2005; Wade and Wood, 2005; Corgne et al., 2008; Kegler et al., 2008; Mann et al., 2009; Ricolleau et al., 2011; Siebert et al., 2011, 2012, 2013; Bouhifd et al., 2013; Tsuno et al., 2013) (Table A.3). Parameterizations dependent only on pressure and temperature were fit to the combined dataset for Ni, Co, Si, and O, while a parameterization that is also dependent on the metallic melt composition is preferred for V and Cr. At low pressures, Ni and Co become less siderophile with increasing temperature, with this trend reversing at ~45 GPa. V and Cr appear highly sensitive to metallic melt composition, in particular to the oxygen and carbon contents of the metal; alternatively, these elements may be in a different valence state at the higher oxygen fugacity conditions of diamond cell experiments. Si and O partitioning are relatively insensitive to pressure, with Si having a stronger temperature dependence than O.

The new parameterizations of these data can be used to learn about the conditions of core formation and the composition of the core. For a single effective pressure and temperature of core formation, we find that the Earth's Ni and Co distributions imply core–mantle equilibration at 54 ± 5 GPa and 3300–3400 K. Silicon and oxygen partitioning are also compatible with equilibration at these *P*–*T* conditions, which result in a core composition that is consistent with the core's measured density (8.5 ± 1.4 wt% Si, 1.6 ± 0.3 wt% O). The core formation process can also be modeled more realistically using multi-stage core growth models, which can approximately match the Earth's Ni and Co distributions and produce a core whose Si and O contents are consistent with its density. The parameterizations for Ni, Co, V, Cr, Si, and O partitioning developed here can serve as inputs into more complex models of Earth's core formation in the future.

ACKNOWLEDGMENTS

R.A.F. acknowledges support from a National Science Foundation (NSF) Graduate Research Fellowship, an Illinois Space Grant Consortium Graduate Research Fellowship, an International Centre for Diffraction Data Ludo Frevel Crystallography Scholarship, and a Plotnick Fellowship from the

University of Chicago. This work was funded by a European Research Council Advanced Grant (contract number 290568) to D.C.R., by the NSF through grants EAR-1243847 and EAR-1427123 to A.J.C., and by the Gottfried Wilhelm Leibniz prize of the Deutsche Forschungsgemeinschaft to F.L. (LA830/14-1).

We thank Leonid Dubrovinsky for useful discussions; Catherine McCammon, Antje Vogel, and Esther Posner for help synthesizing metallic starting materials; Ian Steele for assistance with starting material characterization; Gregory Myers and Elizabeth Thompson for assistance with sample preparation; Bethany Chidester, Daniel Reaman, and Vitali Prakapenka for assistance with diamond anvil cell experiments; and Sylvain Petitgirard for assistance with selection of standards in TEM-EDX and EELS analysis. We also thank Julien Siebert and an anonymous reviewer for constructive reviews, and the editor for handling our manuscript.

APPENDIX A. SUPPLEMENTARY DATA

Supplementary data associated with this article can be found, in the online version, at <http://dx.doi.org/10.1016/j.gca.2015.06.026>.

REFERENCES

- Allègre C. J., Poirier J.-P., Humler E. and Hofmann A. W. (1995) The chemical composition of the Earth. *Earth Planet. Sci. Lett.* **134**, 515–526.
- Andraut D., Bolfan-Casanova N., Lo Nigro G., Bouhifd M. A., Garbarino G. and Mezouar M. (2011) Solidus and liquidus profiles of chondritic mantle: Implication for melting of the Earth across its history. *Earth Planet. Sci. Lett.* **304**, 251–259.
- Asahara Y., Frost D. J. and Rubie D. C. (2007) Partitioning of FeO between magnesiowüstite and liquid iron at high pressures and temperatures: Implications for the composition of the Earth's outer core. *Earth Planet. Sci. Lett.* **257**, 435–449.
- Birch F. (1952) Elasticity and constitution of the Earth's interior. *J. Geophys. Res.* **57**, 227–286.
- Bouchard D. and Bale C. W. (1995) Simultaneous optimization of thermochemical data for liquid iron alloys containing C, N, Ti, Si, Mn, S, and P. *Metall. Mater. Trans. B* **26B**, 467–484.
- Bouhifd M. A. and Jephcoat A. P. (2003) The effect of pressure on partitioning of Ni and Co between silicate and iron-rich metal liquids: a diamond-anvil cell study. *Earth Planet. Sci. Lett.* **209**, 245–255.
- Bouhifd M. A. and Jephcoat A. P. (2011) Convergence of Ni and Co metal–silicate partition coefficients in the deep magma-ocean and coupled silicon–oxygen solubility in iron melts at high pressures. *Earth Planet. Sci. Lett.* **307**, 341–348.
- Bouhifd M. A., Andraut D., Bolfan-Casanova N., Hammouda T. and Devidal J. L. (2013) Metal–silicate partitioning of Pb and U: Effects of metal composition and oxygen fugacity. *Geochim. Cosmochim. Acta* **114**, 13–28.
- Campbell A. J. (2008) Measurement of temperature distributions across laser heated samples by multispectral imaging radiometry. *Rev. Sci. Instrum.* **79**, 015108.
- Campbell A. J., Danielson L., Richter K., Seagle C. T., Wang Y. and Prakapenka V. B. (2009) High pressure effects on the iron–iron oxide and nickel–nickel oxide oxygen fugacity buffers. *Earth Planet. Sci. Lett.* **286**, 556–564.
- Chabot N. L. and Agee C. B. (2003) Core formation in the Earth and Moon: New experimental constraints from V, Cr, and Mn. *Geochim. Cosmochim. Acta* **67**, 2077–2091.
- Chabot N. L., Draper D. S. and Agee C. B. (2005) Conditions of core formation in the Earth: Constraints from Nickel and Cobalt partitioning. *Geochim. Cosmochim. Acta* **69**, 2141–2151.
- Chi H., Dasgupta R., Duncan M. S. and Shimizu N. (2014) Partitioning of carbon between Fe-rich alloy melt and silicate melt in a magma ocean – Implications for the abundance and origin of volatiles in Earth, Mars, and the Moon. *Geochim. Cosmochim. Acta* **139**, 447–471.
- Corgne A., Keshav S., Wood B. J., McDonough W. F. and Fei Y. (2008) Metal–silicate partitioning and constraints on core composition and oxygen fugacity during Earth accretion. *Geochim. Cosmochim. Acta* **72**, 574–589.
- Cottrell E., Walter M. J. and Walker D. (2009) Metal–silicate partitioning of tungsten at high pressure and temperature: Implications for equilibrium core formation in Earth. *Earth Planet. Sci. Lett.* **281**, 275–287.
- Dasgupta R., Chi H., Shimizu N., Buono A. S. and Walker D. (2013) Carbon solution and partitioning between metallic and silicate melts in a shallow magma ocean: Implications for the origin and distribution of terrestrial carbon. *Geochim. Cosmochim. Acta* **102**, 191–212.
- Dresler W. (1989) *Ironmaking Conference Proceedings ISS-AIME*. Warrendale, Pennsylvania. pp. 83–87.
- Fischer R. A. and Campbell A. J. (2010) High-pressure melting of wüstite. *Am. Mineral.* **95**, 1473–1477.
- Fischer R. A. and Ciesla F. J. (2014) Dynamics of the terrestrial planets from a large number of *N*-body simulations. *Earth Planet. Sci. Lett.* **392**, 28–38.
- Fischer R. A., Campbell A. J., Shofner G. A., Lord O. T., Dera P. and Prakapenka V. B. (2011) Equation of state and phase diagram of FeO. *Earth Planet. Sci. Lett.* **304**, 496–502.
- Fischer R. A., Campbell A. J., Caracas R., Reaman D. M., Heinz D. L., Dera P. and Prakapenka V. B. (2014) Equations of state in the Fe–FeSi system at high pressures and temperatures. *J. Geophys. Res.* **119**, 2810–2827.
- Frost D. J., Asahara Y., Rubie D. C., Miyajima N., Dubrovinsky L. S., Holzapfel C., Ohtani E., Miyahara M. and Sakai T. (2010) Partitioning of oxygen between the Earth's mantle and core. *J. Geophys. Res.* **115**, B02202.
- Geßmann C. K. and Rubie D. C. (1998) The effect of temperature on the partitioning of nickel, cobalt, manganese, chromium, and vanadium at 9 GPa and constraints on formation of the Earth's core. *Geochim. Cosmochim. Acta* **62**, 867–882.
- Hillgren V. J., Drake M. J. and Rubie D. C. (1996) High pressure and high temperature metal–silicate partitioning of siderophile elements: The importance of silicate liquid composition. *Geochim. Cosmochim. Acta* **60**, 2257–2263.
- Ito E., Morooka K., Ujike O. and Katsura T. (1995) Reactions between molten iron and silicate melts at high pressure: Implications for the chemical evolution of Earth's core. *J. Geophys. Res.* **100**, 5901–5910.
- Jana D. and Walker D. (1997) The impact of carbon on element distribution during core formation. *Geochim. Cosmochim. Acta* **61**, 2759–2763.
- Japan Society for the Promotion of Science and the Nineteenth Committee on Steelmaking (1988) *Steelmaking Data Sourcebook*. Gordon and Breach Science Publishers, New York, pp. 273–297.
- Jeanloz R. and Ahrens T. J. (1980) Equations of state of FeO and CaO. *Geophys. J. R. Astron. Soc.* **62**, 505–528.
- Kawazoe T. and Ohtani E. (2006) Reaction between liquid iron and (Mg,Fe)SiO₃-perovskite and solubilities of Si and O in molten iron at 27 GPa. *Phys. Chem. Mineral.* **33**, 227–234.
- Kegler Ph., Holzheid A., Frost D. J., Rubie D. C., Dohmen R. and Palme H. (2008) New Ni and Co metal–silicate partitioning

- data and their relevance for an early terrestrial magma ocean. *Earth Planet. Sci. Lett.* **268**, 28–40.
- Li J. and Agee C. B. (1996) Geochemistry of mantle–core differentiation at high pressure. *Nature* **381**, 686–689.
- Li J. and Agee C. B. (2001) The effect of pressure, temperature, oxygen fugacity and composition on partitioning of nickel and cobalt between liquid Fe–Ni–S alloy and liquid silicate: Implications for the Earth's core formation. *Geochim. Cosmochim. Acta* **65**, 1821–1832.
- Li Y., Dasgupta R. and Tsuno K. (2015) The effects of sulfur, silicon, water, and oxygen fugacity on carbon solubility and partitioning on Fe-rich alloy and silicate melt systems at 3 GPa and 1600 °C: Implications for core–mantle differentiation and degassing of magma oceans and reduced planetary mantles. *Earth Planet. Sci. Lett.* **415**, 54–66.
- Lin J.-F., Campbell A. J., Heinz D. L. and Shen G. (2003) Static compression of iron–silicon alloys: Implication for silicon in the Earth's core. *J. Geophys. Res.* **108**, 2045.
- Ma Z. (2001) Thermodynamic description for concentrated metallic solutions using interaction parameters. *Metall. Mater. Trans. B* **32B**, 87–103.
- Malavergne V., Siebert J., Guyot F., Gautron L., Combes R., Hammouda T., Borensztajn S., Frost D. and Martinez I. (2004) Si in the core? New high-pressure and high-temperature experimental data. *Geochim. Cosmochim. Acta* **68**, 4201–4211.
- Mann U., Frost D. J. and Rubie D. C. (2009) Evidence for high-pressure core–mantle differentiation from the metal–silicate partitioning of lithophile and weakly-siderophile elements. *Geochim. Cosmochim. Acta* **73**, 7360–7386.
- Mao H. K., Bell P. M., Shaner J. W. and Steinberg D. J. (1978) Specific volume measurements of Cu, Mo, Pd, and Ag and calibration of the ruby R_1 fluorescence pressure gauge from 0.06 to 1 Mbar. *J. Appl. Phys.* **49**, 3276–3283.
- Mao Z., Lin J.-F., Liu J., Alatas A., Gao L., Zhao J. and Mao H.-K. (2012) Sound velocities of Fe and Fe–Si alloy in the Earth's core. *Proc. Natl. Acad. Sci. U.S.A.* **109**, 10239–10244.
- McDonough W. F. (2003) Compositional model for the Earth's core. In *Treatise on Geochemistry*, vol. 2 (ed. R. W. Carlson). Elsevier, Oxford, pp. 547–568.
- McDonough W. F. and Sun S.-S. (1995) The composition of the Earth. *Chem. Geol.* **120**, 223–253.
- Miyajima N., Holzappel C., Asahara Y., Dubrovinsky L., Frost D. J., Rubie D. C., Drechsler M., Niwa K., Ichihara M. and Yagi T. (2009) Combining FIB milling and conventional Argon ion milling techniques to prepare high-quality site-specific TEM samples for quantitative EELS analysis of oxygen in molten iron. *J. Microsc.* **238**, 200–209.
- Morard G., Siebert J., Andrault D., Guignot N., Garbarino G., Guyot F. and Antonangeli D. (2013) The Earth's core composition from high pressure density measurements of liquid iron alloys. *Earth Planet. Sci. Lett.* **373**, 169–178.
- O'Neill H. St. C., Canil D. and Rubie D. C. (1998) Oxide-metal equilibria to 2500 °C and 25 GPa: Implications for core formation and the light component in the Earth's core. *J. Geophys. Res.* **103**, 12239–12260.
- Ohtani E., Yurimoto H. and Seto S. (1997) Element partitioning between metallic liquid, silicate liquid, and lower-mantle minerals: Implications for core formation of the Earth. *Phys. Earth Planet. Inter.* **100**, 97–114.
- Ozawa H., Hirose K., Mitome M., Bando Y., Sata N. and Ohishi Y. (2008) Chemical equilibrium between ferropicrinite and molten iron to 134 GPa and implications for iron content at the bottom of the mantle. *Geophys. Res. Lett.* **35**, L05308.
- Ozawa H., Hirose K., Mitome M., Bando Y., Sata N. and Ohishi Y. (2009) Experimental study of reaction between perovskite and molten iron to 146 GPa and implications for chemically distinct buoyant layer at the top of the core. *Phys. Chem. Mineral.* **36**, 355–363.
- Palme H., Kegler P., Holzheid A., Frost D. J. and Rubie D. C. (2011) Comment on “Prediction of metal–silicate partition coefficients for siderophile elements: An update and assessment of PT conditions for metal–silicate equilibrium during accretion of the Earth” by K. Righter, EPSL 304 (2011) 158–167, 2011. *Earth Planet. Sci. Lett.* **312**, 516–518.
- Poirier J.-P. (1994) Light elements in the Earth's outer core: A critical review. *Phys. Earth Planet. Inter.* **85**, 319–337.
- Raymond S. N., Quinn T. and Lunine J. I. (2006) High-resolution simulations of the final assembly of Earth-like planets I. Terrestrial accretion and dynamics. *Icarus* **183**, 265–282.
- Ricolleau A., Fei Y., Corgne A., Siebert J. and Badro J. (2011) Oxygen and silicon contents of Earth's core from high pressure metal–silicate partitioning experiments. *Earth Planet. Sci. Lett.* **310**, 409–421.
- Righter K. (2003) Metal–silicate partitioning of siderophile elements and core formation in the early Earth. *Annu. Rev. Earth Planet. Sci.* **31**, 135–174.
- Righter K. (2011) Prediction of metal–silicate partition coefficients for siderophile elements: An update and assessment of PT conditions for metal–silicate equilibrium during accretion of the Earth. *Earth Planet. Sci. Lett.* **304**, 158–167.
- Righter (2015) Modeling siderophile elements during core formation and accretion, and the role of the deep mantle and volatiles. *Am. Mineral.* **100**, 1098–1109.
- Righter K., Drake M. J. and Yaxley G. (1997) Prediction of siderophile element metal–silicate partition coefficients to 20 GPa and 2800 °C: the effects of pressure, temperature, oxygen fugacity, and silicate and metallic melt compositions. *Phys. Earth Planet. Inter.* **100**, 115–134.
- Righter K., Pando K. M., Danielson L. and Lee C.-T. (2010) Partitioning of Mo, P and other siderophile elements (Cu, Ga, Sn, Ni Co, Cr, Mn, V, and W) between metal and silicate melt as a function of temperature and silicate melt composition. *Earth Planet. Sci. Lett.* **291**, 1–9.
- Righter K., King C., Danielson L., Pando K. and Lee C. T. (2011) Experimental determination of the metal/silicate partition coefficient of Germanium: Implications for core and mantle differentiation. *Earth Planet. Sci. Lett.* **304**, 379–388.
- Ringwood A. E. (1959) On the chemical evolution and densities of the planets. *Geochim. Cosmochim. Acta* **15**, 257–283.
- Rubie D. C., Melosh H. J., Reid J. E., Liebske C. and Righter K. (2003) Mechanisms of metal–silicate equilibration in the terrestrial magma ocean. *Earth Planet. Sci. Lett.* **205**, 239–255.
- Rubie D. C., Frost D. J., Mann U., Asahara Y., Nimmo F., Tsuno K., Kegler P., Holzheid A. and Palme H. (2011) Heterogeneous accretion, composition and core–mantle differentiation of the Earth. *Earth Planet. Sci. Lett.* **301**, 31–42.
- Rubie D. C., Jacobson S. A., Morbidelli A., O'Brien D. P., Young E. D., de Vries J., Nimmo F., Palme H. and Frost D. J. (2015a) Accretion and differentiation of the terrestrial planets with implications for the composition of early-formed Solar System bodies and accretion of water. *Icarus* **248**, 89–108.
- Rubie D. C., Nimmo F. and Melosh H. J. (2015b) Formation of the Earth's core. In *Treatise on Geophysics*, vol. 9, 2nd ed (ed. G. Schubert). Elsevier, Oxford, pp. 43–79.
- Sanloup C., van Westrenen W., Dasgupta R., Maynard-Casely H. and Perrillat J.-P. (2011) Compressibility change in iron-rich melt and implications for core formation models. *Earth Planet. Sci. Lett.* **306**, 118–122.
- Sata N., Hirose K., Shen G., Nakajima Y., Ohishi Y. and Hirao N. (2010) Compression of FeSi, Fe₃C, Fe_{0.95}O, and FeS under the core pressures and implication for light element in the Earth's core. *J. Geophys. Res.* **115**, B09204.

- Shibaev S. S. and Grigorovich K. V. (2008) Solubility of oxygen in iron–silicon melts. *J. Phys. Conf. Ser.* **98**, 032012.
- Siebert J., Corgne A. and Ryerson F. J. (2011) Systematics of metal–silicate partitioning for many siderophile elements applied to Earth's core formation. *Geochim. Cosmochim. Acta* **75**, 1451–1489.
- Siebert J., Badro J., Antonangeli D. and Ryerson F. J. (2012) Metal–silicate partitioning of Ni and Co in a deep magma ocean. *Earth Planet. Sci. Lett.* **321–322**, 189–197.
- Siebert J., Badro J., Antonangeli D. and Ryerson F. J. (2013) Terrestrial accretion under oxidizing conditions. *Science* **339**, 1194–1197.
- Takafuji N., Hirose K., Mitome M. and Bando Y. (2005) Solubilities of O and Si in liquid iron in equilibrium with (Mg,Fe)SiO₃ perovskite and the light elements in the core. *Geophys. Res. Lett.* **32**, L06313.
- Tateno S., Kuwayama Y., Hirose K. and Ohishi Y. (2015) The structure of Fe–Si alloy in Earth's inner core. *Earth Planet. Sci. Lett.* **418**, 11–19.
- Thibault Y. and Walter M. J. (1995) The influence of pressure and temperature on the metal–silicate partition coefficients of nickel and cobalt in a model C1 chondrite and implications for metal segregation in a deep magma ocean. *Geochim. Cosmochim. Acta* **59**, 991–1002.
- Tsuno K., Frost D. J. and Rubie D. C. (2013) Simultaneous partitioning of silicon and oxygen into the Earth's core during early Earth differentiation. *Geophys. Res. Lett.* **40**, 66–71.
- Tuff J., Wood B. J. and Wade J. (2011) The effect of Si on metal–silicate partitioning of siderophile elements and implications for the conditions of core formation. *Geochim. Cosmochim. Acta* **75**, 673–690.
- van Cappellen E. (1990) The parameterless correction method in X-ray microanalysis. *Microsc. Microanal. Microstruct.* **1**, 1–22.
- Wade J. and Wood B. J. (2005) Core formation and the oxidation state of the Earth. *Earth Planet. Sci. Lett.* **236**, 78–95.
- Wade J. and Wood B. J. (2012) Metal–silicate partitioning experiments in the diamond anvil cell: A comment on potential analytical errors. *Phys. Earth Planet. Inter.* **192–193**, 54–58.
- Wade J., Wood B. J. and Tuff J. (2012) Metal–silicate partitioning of Mo and W at high pressures and temperatures: Evidence for late accretion of sulphur to the Earth. *Geochim. Cosmochim. Acta* **85**, 58–74.
- Walker D., Dasgupta R., Li J. and Buono A. (2013) Nonstoichiometry and growth of some Fe carbides. *Contrib. Mineral. Petrol.* **166**, 935–957.
- Walter M. J. and Cottrell E. (2013) Assessing uncertainty in geochemical models for core formation in Earth. *Earth Planet. Sci. Lett.* **365**, 165–176.
- Wood B. J., Walter M. J. and Wade J. (2006) Accretion of the Earth and segregation of its core. *Nature* **441**, 825–833.
- Wood B. J., Wade J. and Kilburn M. R. (2009) Core formation and the oxidation state of the Earth: Additional constraints from Nb, V and Cr partitioning. *Geochim. Cosmochim. Acta* **72**, 1415–1426.
- Wood B. J., Kiseeva E. S. and Mirolo F. J. (2014) Accretion and core formation: The effects of sulfur on metal–silicate partition coefficients. *Geochim. Cosmochim. Acta* **145**, 248–267.
- Zhang Y., Sekine T., He H., Yu Y., Liu F. and Zhang M. (2014) Shock compression of Fe–Ni–Si system to 280 GPa: Implications for the composition of the Earth's outer core. *Geophys. Res. Lett.* **41**, 4554–4559.

Associate editor: Rajdeep Dasgupta